Stokes flow in logarithmic-viscosity space: velocity renormalization and a reference-operator formulation

Alessandro Forte[1,2] and Shayan Kamali Lima[1]

[1] Institut de Physique du Globe de Paris, 75238 Paris Cedex 05, France

[2] Department of Geological Sciences, University of Florida, Gainesville, Florida, USA

Corresponding author: Alessandro Forte, `forte@ufl.edu`, `forte@ipgp.fr`

Preprint status. This manuscript is a non-peer-reviewed preprint submitted to EarthArXiv. It has also been submitted to the *Journal of Fluid Mechanics* for peer review.

August 2026

Banner appropriate to article type will appear here in typeset article

Stokes flow in logarithmic-viscosity space: velocity renormalization and a reference-operator formulation

Alessandro Forte[1,2], Shayan Kamali Lima[1]

[1]Institut de Physique du Globe de Paris, 75238 Paris Cedex 05, FRANCE

[2]University of Florida, Department of Geological Sciences, Gainesville, FL, USA

Corresponding author: Alessandro Forte, forte@ufl.edu, forte@ipgp.fr

(Received xx; revised xx; accepted xx)

Effective viscosity in crystalline solids commonly depends exponentially on temperature, pressure, composition and other state variables, producing spatial variations over many orders of magnitude and making variable-viscosity Stokes flow numerically demanding. We develop an exact, coordinate-independent reformulation using logarithmic viscosity $\varLambda = \ln(\eta/\eta_0)$ and renormalized velocity $\mathbf{v} = (\eta/\eta_0)\mathbf{u}$. The transformation identifies $\boldsymbol{\xi} = \nabla\varLambda$ as the local measure of viscosity heterogeneity: its magnitude and direction determine how spatial viscosity variations modify the flow, while the absolute viscosity scale controls conversion back to the physical velocity. Multiplicative viscosity contrasts thereby become additive variations in $\varLambda$, and a fixed-reference-viscosity Stokes operator can be retained. Viscosity heterogeneity enters through coupling terms constructed from $\mathbf{v}$ and $\boldsymbol{\xi}$ together with a corresponding transformed mass-conservation source. We verify the formulation with an exact manufactured solution, a two-region Cartesian benchmark and a three-dimensional spherical-shell calculation with lateral viscosity contrast 10^4. In the spherical test, viscosity heterogeneity redistributes a simple buoyancy-driven poloidal response into broad-spectrum poloidal and toroidal flow contributions whose harmonic content agrees with theoretically predicted selection rules. The degeneracy related to the degree-one toroidal mode is resolved by imposing zero angular momentum on the reconstructed physical flow, while preserving dynamically forced differential rotation. Therefore, compared to an isoviscous reference solution, the variable-viscosity case develops substantial shorter-wavelength surface divergence and radial vorticity. The strong-viscosity-contrast calculation converges in 49 fixed-point updates, and spectral, resolution and physical-field reconstruction tests confirm that theoretically-predicted flow couplings are resolved.

Key words: Stokes flow; spatially variable viscosity; logarithmic viscosity; velocity renormalization; pseudo-stress; reference-operator formulation; poloidal–toroidal coupling; spherical harmonics; geophysical fluid dynamics

Abstract must not spill onto p.2

1. Introduction

The effective viscosity characterizing creeping flows in crystalline solids is rarely uniform. In such solids, deformation is controlled by thermally activated processes involving point defects, diffusion, dislocations and grain boundaries. Temperature and pressure therefore enter the constitutive behaviour through exponential factors, while composition, grain size, volatile content and mineral phase can introduce further large variations (Poirier 1985; Karato 2008). In planetary interiors, effective viscosity may span many orders of magnitude and exerts a fundamental control on convection, horizontal surface motions, gravity anomalies and the vertical displacement of material boundaries (Richards & Hager 1989; Zhang & Christensen 1993; Čadek & Fleitout 2003; Kaban *et al.* 2007; Moucha *et al.* 2007).

The exponential character of these rheologies points naturally to logarithmic viscosity as the variable that measures spatial heterogeneity, which we define as follows:

$$\Lambda = \ln\left(\frac{\eta}{\eta_0}\right), \qquad \boldsymbol{\xi} = \nabla\Lambda = \frac{\nabla\eta}{\eta},$$

where η_0 is a chosen reference viscosity. The vector $\boldsymbol{\xi}$ measures the local fractional change of viscosity and retains its magnitude and direction under any uniform rescaling of the complete viscosity field. It is therefore independent of the arbitrary overall viscosity scale. A multiplicative viscosity contrast becomes an additive change in Λ; a contrast W, for example, corresponds to the change $\Delta\Lambda = \ln W$. These simple properties become much more consequential after the Stokes equations are transformed. They reveal $\boldsymbol{\xi}$, rather than the dimensional gradient $\nabla\eta$, as the natural local measure of spatial viscosity variations that modulates flow.

This distinction separates two physical roles that are intertwined in the usual form of the Stokes equations. The absolute viscosity scale controls the relation between stress and physical velocity. The spatial modulation of flow associated with viscosity heterogeneity depends on how rapidly, and in what direction, the logarithm of viscosity varies. A uniform multiplication of viscosity changes the amplitude of the physical velocity without changing $\boldsymbol{\xi}$. The transformed formulation developed here makes this separation explicit.

Strong spatial viscosity variations create a difficult numerical problem in the conventional equations. Viscosity multiplies the strain rate in the stress tensor, so its full spatial amplitude remains embedded in the momentum operator. Large contrasts can produce poorly scaled discrete systems and increase sensitivity to coefficient interpolation, grid resolution, boundary treatment and the choice of linear solver. Similar difficulties arise in other slowly moving fluids with strong spatial variations in viscosity, including glacial isostatic adjustment, flow through porous and fractured media, and transport in industrial and biological fluids (Blank *et al.* 2021; Lau *et al.* 2018; Eberhard *et al.* 2020; Rodríguez de Castro & Goyeau 2021; Belfort & Younes 2025; De Vanna *et al.* 2021).

The effects of spatially variable viscosity on Stokes flow have been studied extensively. Early numerical calculations in two- and three-dimensional geometries demonstrated how strongly lateral viscosity variations can modify flow and its surface expression (Richards & Hager 1989; Christensen & Harder 1991; Zhang & Christensen 1993). Related selection rules for poloidal–toroidal coupling caused by lateral stiffness variations in a thin lithospheric shell were derived by Ribe (1992), while Forte & Peltier (1994) developed the generalized-spherical-harmonic coupling framework for arbitrary three-dimensional mantle viscosity variations. Later studies developed increasingly complete treatments of lateral viscosity structure in spherical, compressible and self gravitating mantle flow (Čadek & Fleitout 2003, 2006; Kaban *et al.* 2007; Moucha *et al.* 2007; Petrunin *et al.* 2013; Rogozhina 2008). These studies established both the physical importance of viscosity heterogeneity and the numerical demands of solving the resulting variable coefficient equations. Iterative spherical spectral methods were subsequently extended to increasingly strong lateral viscosity contrasts, although their convergence becomes progressively more demanding (Čadek & Fleitout 2003; Petrunin *et al.* 2013).

A complementary line of work recognized that much of the difficulty created by spatially varying viscosity can be reorganized by scaling the velocity and expressing viscosity variations through derivatives of its logarithm. In an early three-dimensional spherical formulation, Zhang & Christensen (1993) introduced velocity variables scaled by viscosity relative to a radial reference profile and showed that the corresponding viscous-load terms involve spatial derivatives of the logarithm of this viscosity ratio. Related constructions appeared in Colin (1993) and were developed further in later effective-load formulations (Karpychev & Fleitout 2000; Čadek & Fleitout 2003; Rogozhina 2008). For a fixed reference viscosity, the corresponding relative viscosity gradient is

$$\nabla \ln \left(\frac{\eta}{\eta_0} \right) = \nabla \ln \eta = \frac{\nabla \eta}{\eta}.$$

For example, the spectral formulation of Karpychev & Fleitout (2000) expresses the viscous load through products that couple $\nabla \ln \eta$ to a viscosity-scaled velocity, while Čadek & Fleitout (2003) explicitly introduces a scaled velocity together with $\boldsymbol{\xi} = \nabla \ln(\eta/\eta_0)$ to stabilize the iterative solution at large lateral viscosity contrast. Forte (2000) employed viscosity scaled flow variables for a radially varying viscosity. The scaling yields radial equations in which spatial changes in viscosity appear through derivatives of its logarithm.

These earlier results contain the essential mathematical insight on which the present work builds. Our aim is to expose its full three-dimensional structure and physical meaning. We show that, for an arbitrary prescribed positive Newtonian viscosity field, logarithmic viscosity and the corresponding renormalized velocity arise from an exact change of variables in the Stokes equations. The transformation identifies

$$\boldsymbol{\xi} = \nabla \ln \left(\frac{\eta}{\eta_0} \right) = \frac{\nabla \eta}{\eta}$$

as the natural local measure of viscosity heterogeneity. The magnitude and geometry of this field govern the coupling produced by spatial viscosity variations, while the absolute viscosity scale determines the conversion between the renormalized and physical velocities. This distinction provides the basis for a unified reference-operator formulation in which a fixed reference-viscosity Stokes operator is retained, while the constitutive relation, momentum equation, mass constraint and boundary conditions are transformed consistently. This transformation will be carried out at the tensor level, independently of coordinate system. The complete viscosity-dependent contribution to the transformed constitutive law will thereby be collected into a single symmetric, traceless pseudo-stress tensor. The divergence of this tensor supplies the heterogeneous-viscosity-induced momentum coupling.

The starting point for our treatment is the replacement of physical velocity $\mathbf{u}$ by the renormalized velocity

$$\mathbf{v} = \left(\frac{\eta}{\eta_0} \right) \mathbf{u}.$$

When this variable is substituted into the strain rate, derivatives of the viscosity scaling appear only through $\boldsymbol{\xi} = \nabla \Lambda$. The same field enters the transformed mass-conservation equation. Thus, the gradient of logarithmic viscosity is not an auxiliary parameter. Rather, it emerges directly from the exact change of variables as the field that controls the geometry and strength of viscosity induced flow coupling in the transformed equations. Absolute viscosity still determines the conversion from $\mathbf{v}$ back to the physical velocity $\mathbf{u}$; the heterogeneous flow coupling itself is organized by $\boldsymbol{\xi}$.

The principal mathematical contribution of this paper is a coordinate independent derivation of the resulting three dimensional constitutive relation, mass-conservation constraint and momentum-conservation equation. For a prescribed positive Newtonian viscosity field, the transformation is exact when the boundary conditions are transformed consistently. A reference viscosity or reference viscosity profile can then be chosen so that the corresponding Stokes operator is retained. The remaining heterogeneity enters through pseudo-loading terms that act linearly on the renormalized velocity and depend on $\boldsymbol{\xi}$. In a numerical implementation, these terms can be evaluated as an effective load acting in addition to the primary buoyancy force, along with an associated source term in the transformed mass-conservation equation. Large multiplicative contrasts in viscosity are therefore represented through logarithmic variation and its spatial gradient, rather than being carried in full amplitude by the reference operator.

The problem remains linear when viscosity is prescribed. If viscosity depends on an evolving quantity such as stress or strain rate, the transformed Stokes solve becomes one component of a broader nonlinear rheological iteration. The present work concentrates on the prescribed viscosity problem so that the mathematical structure of the transformation and its numerical consequences can be isolated cleanly.

We assess the formulation in three complementary settings. An exact manufactured solution in Cartesian geometry tests the transformed equations and their discretization directly. Next, a two-region Cartesian calculation tests the redistribution of flow across a strong viscosity contrast and provides a controlled comparison with the particular direct discretization used in this study. Finally, a spherical shell calculation then combines a simple buoyancy forcing with a harmonic representation of the lateral viscosity gradient that represents a factor 10^4 contrast in viscosity. This final problem is designed to expose the three dimensional coupling generated by $\boldsymbol{\xi} = \nabla \ln(\eta/\eta_0)$. The resulting poloidal and toroidal flows are compared directly with the generalized spherical harmonic selection rules of Forte & Peltier (1994). Furthermore, the targeted radial and angular refinement tests determine whether the generated spectral bandwidth is numerically resolved.

The paper is organized as follows. Section 2 develops the physical meaning of the renormalized velocity, logarithmic viscosity and its gradient, and establishes the separation between overall viscosity scale and spatial heterogeneity. Section 3 derives the transformed governing equations, the decomposition into a fixed reference-viscosity Stokes operator and explicit viscosity-heterogeneity coupling terms, and the corresponding boundary conditions. Section 3.8 then specializes the formulation to three-dimensional spherical-shell geometry, developing its vector-spherical-harmonic representation, poloidal–toroidal coupling structure and reference Green-function solution. Section 4 presents the numerical implementation and the three validation and illustrative calculations, including the strong lateral viscosity variations in a spherical shell. Section 5 summarizes the principal implications of the formulation, its domain of applicability and limitations, and possible extensions to more general heterogeneous Stokes-flow problems.

2. Velocity renormalization and the emergence of logarithmic viscosity

The formulation developed in this paper is based on two related changes of variable. The first rescales the physical velocity by the local viscosity relative to a fixed reference value. The second represents viscosity through its logarithm. These transformations address different aspects of the same problem. Rescaled velocity separates the overall viscosity scale from the influence of its spatial variation, whereas the logarithmic viscosity provides a natural description of rheologies in which several physical effects combine multiplicatively. We introduce their physical meaning here before deriving the transformed governing equations in Section 3.

2.1. *Large viscosity contrasts in thermally activated rheology*

The strong viscosity variations found in crystalline materials arise from the microscopic processes that permit deformation. Diffusion, dislocation motion, grain boundary processes and the creation and migration of defects are thermally activated. Their rates therefore depend exponentially on activation energy and pressure, while grain size, water content, composition and mineral phase may introduce additional multiplicative factors (Poirier 1985; Karato 2008).

A schematic creep relation that includes several of these effects may be written as

$$\dot{\varepsilon} = A\,\sigma^n d^{-m} C^r_{\mathrm{H_2O}} \exp\left[-\frac{E^* + PV^*}{RT}\right], \tag{2.1}$$

where $\dot{\varepsilon}$ and σ denote representative measures of strain rate and stress, A is a material coefficient, n is the stress exponent, d is grain size, m is the grain size exponent, $C_{\mathrm{H_2O}}$ measures water content, and r is its exponent. The quantities E^* and V^* are the activation energy and activation volume, while P, T and R denote pressure, temperature and the gas constant.

For Newtonian creep, $n = 1$, the corresponding viscosity has the schematic dependence

$$\eta \propto A^{-1} d^m C^{-r}_{\mathrm{H_2O}} \exp\left[\frac{E^* + PV^*}{RT}\right]. \tag{2.2}$$

Taking the logarithm converts these multiplicative contributions into additive terms:

$$\ln\eta = \text{constant} - \ln A + m\ln d - r\ln C_{\mathrm{H_2O}} + \frac{E^* + PV^*}{RT}. \tag{2.3}$$

The emergence of a logarithmic representation of viscosity, via the viscosity renormalization of the flow velocity (described next), therefore provides a natural constitutive variable in which several independent micro-physical contributions to viscous resistance can be represented additively.

2.2. *Renormalization of the velocity field*

The key change of variable that transforms the Stokes flow equations is

$$\mathbf{v} = \frac{\eta}{\eta_0}\mathbf{u}, \tag{2.4}$$

where $\mathbf{u}$ is the physical velocity, $\eta(\mathbf{x})$ is the prescribed viscosity field and η_0 is a fixed reference viscosity. We refer to $\mathbf{v}$ as the renormalized velocity. Closely related viscosity-scaled velocity variables have appeared in earlier formulations of mantle flow with radial and lateral viscosity variations (Zhang & Christensen 1993; Colin 1993; Karpychev & Fleitout 2000; Forte 2000; Čadek & Fleitout 2003; Rogozhina 2008). Its physical role is most clearly understood by considering how a Stokes solution responds when the entire viscosity field is multiplied by the same constant.

For a fixed spatial viscosity pattern, an increase in the overall viscosity scale reduces the amplitude of the physical velocity. The factor η/η_0 in (2.4) removes this leading reciprocal dependence from the transformed velocity. The field $\mathbf{v}$ therefore emphasizes the structure of the flow associated with the spatial pattern of viscosity, whereas the conversion back to $\mathbf{u}$ restores the dependence on the absolute viscosity scale.

We emphazsize that equation (2.4) is a change of dependent variable, not a local constitutive relation. Therefore, it should not be understood to imply that the physical velocity at a point is determined only by the viscosity at that point. Stokes flow is elliptic and nonlocal: the velocity depends on the forcing, pressure, geometry, boundary conditions and viscosity throughout the domain. The transformation instead identifies a global scaling property of the complete solution.

The viscosity scale η_0 may be chosen to suit the physical problem or the numerical method. It may, for example, be a representative viscosity of the domain or the viscosity associated with an existing reference Stokes solver. Changing η_0 changes the normalization of $\mathbf{v}$, but not the physical velocity recovered from

$$\mathbf{u} = \frac{\eta_0}{\eta}\mathbf{v}. \tag{2.5}$$

The constant η_0 serves only as an arbitrary viscosity scale. It makes the ratio η/η_0 dimensionless, gives the renormalized velocity the same physical dimensions as $\mathbf{u}$, and does not affect the recovered physical solution.

2.3. *Emergence of the logarithmic viscosity gradient*

As will be shown is Section 3, the viscosity renormalizaion of the flow field natural leads to the emergence of a dimensionless logarithmic viscosity

$$\Lambda(\mathbf{x}) = \ln\left[\frac{\eta(\mathbf{x})}{\eta_0}\right], \tag{2.6}$$

where $\eta(\mathbf{x}) > 0$ is the prescribed viscosity field and $\eta_0 > 0$ is a fixed viscosity scale. The value of η_0 sets the normalization but does not alter the spatial derivatives of Λ. This normalization scale should be distinguished from a chosen reference viscosity field,

$$\eta_{\mathrm{ref}}(\mathbf{x}) = \eta_0 \exp\left[\Lambda_{\mathrm{ref}}(\mathbf{x})\right], \tag{2.7}$$

which may retain part of the spatial viscosity structure within the reference Stokes operator. Section 3 develops the exact decomposition of the full viscosity field into this reference part and the remaining spatial variation.

If the viscosity varies between $\eta_{\min}$ and $\eta_{\max}$, its contrast is

$$C_\eta = \frac{\eta_{\max}}{\eta_{\min}}. \tag{2.8}$$

The corresponding range in logarithmic viscosity is

$$\Delta\Lambda = \ln\left(\frac{\eta_{\max}}{\eta_{\min}}\right) = \ln C_\eta. \tag{2.9}$$

Thus, a viscosity ratio that spans several orders of magnitude is represented by an additive logarithmic interval. The importance of this additivity was clearly evident in expression 2.3.

The spatial derivative of logarithmic viscosity is

$$\nabla\varLambda = \frac{\nabla\eta}{\eta}. \tag{2.10}$$

The transformed equations therefore involve the relative rate at which viscosity changes in space, rather than the dimensional gradient $\nabla\eta$ alone. This distinction is important when comparable fractional changes occur in regions with very different absolute viscosities.

These properties do not imply that $\varLambda$ is always smoother than η. A discontinuity in viscosity remains a discontinuity after taking the logarithm, and sharp interfaces still require an appropriate weak or conservative treatment. The exact advantages of the logarithmic variable are the compression of a large positive range, the additive representation of multiplicative rheological factors, and the appearance of the relative gradient $\nabla\eta/\eta$. Any further improvement in numerical conditioning or accuracy depends on the discretization and must be assessed empirically.

2.4. *Separation of the overall viscosity scale from its spatial variation*

Consider a prescribed viscosity field $\eta(\mathbf{x})$ and a Stokes problem with fixed body forces and compatible homogeneous boundary conditions. The deviatoric stress has the form

$$\boldsymbol{\tau} = \eta\,\mathsf{D}(\mathbf{u}), \tag{2.11}$$

where D denotes the linear Newtonian strain rate operator. Its precise form will be given in Section 3.

Suppose that the viscosity field is uniformly rescaled according to

$$\eta'(\mathbf{x}) = c\,\eta(\mathbf{x}), \qquad c > 0. \tag{2.12}$$

The corresponding physical velocity is

$$\mathbf{u}' = \frac{1}{c}\mathbf{u}. \tag{2.13}$$

Because the strain rate operator is linear,

$$\eta'\mathsf{D}(\mathbf{u}') = c\eta\,\mathsf{D}\left(\frac{\mathbf{u}}{c}\right) = \eta\mathsf{D}(\mathbf{u}). \tag{2.14}$$

The viscous stress is therefore unchanged. The pressure field is likewise unchanged, apart from its arbitrary additive constant, and the same force balance is recovered. This is the scale invariance identified for radial mantle flow by Forte (2000), here stated for an arbitrary spatial viscosity pattern.

With the reference viscosity η_0 held fixed, the logarithmic viscosity transforms as

$$\varLambda' = \ln\left(\frac{c\eta}{\eta_0}\right) = \varLambda + \ln c. \tag{2.15}$$

Its gradient is consequently invariant:

$$\nabla\varLambda' = \nabla\varLambda. \tag{2.16}$$

The renormalized velocity is also invariant:

$$\mathbf{v}' = \frac{\eta'}{\eta_0}\mathbf{u}' = \frac{c\eta}{\eta_0}\frac{\mathbf{u}}{c} = \mathbf{v}. \tag{2.17}$$

The three scaling relations may therefore be summarized as

$$\eta \mapsto c\eta, \qquad \mathbf{u} \mapsto \frac{\mathbf{u}}{c}, \qquad \mathbf{v} \mapsto \mathbf{v}, \qquad \nabla\varLambda \mapsto \nabla\varLambda. \tag{2.18}$$

This result separates two roles played by viscosity in an instantaneous Stokes problem. The overall viscosity scale determines the amplitude of the physical velocity, while the normalized flow and the viscous stresses depend on the spatial structure of the viscosity field through logarithmic viscosity and its derivatives. The separation is exact under the assumptions stated above.

Several qualifications are important. First, the result concerns a uniform multiplication of the complete viscosity field. It does not imply a pointwise relation between local velocity and local viscosity. Second, prescribed nonzero velocities or other boundary data that impose an independent velocity scale may not be compatible with (2.13). Third, in a time dependent or fully coupled problem, changing the viscosity scale changes the rate at which temperature, composition and material interfaces evolve. The instantaneous scaling property remains useful, but the later state of the system need not remain unchanged.

The two transformations introduced in this section reveal the central structure of the formulation. The renormalization of velocity by relative viscosity removes the leading dependence on the overall viscosity scale, while the gradient of logarithmic viscosity represents the relative spatial variation of rheology. In the next section we use these variables to derive the exact transformed constitutive, momentum and mass conservation equations, and to show how viscosity variation may be incorporated via the specification of a chosen reference Stokes operator.

3. Exact transformed Stokes equations

We now derive the equations that result from the velocity renormalization introduced in Section 2. The derivation is first presented for a general body force. Buoyancy and self gravity are introduced later as a specialization for planetary interiors.

Throughout this section, the viscosity $\eta(\mathbf{x}) > 0$ is prescribed and Newtonian, and $\eta_0 > 0$ is a constant reference viscosity scale. We initially assume that the viscosity is positive and sufficiently differentiable for all spatial derivatives used below to be defined pointwise. Piecewise smooth and discontinuous viscosity fields require the corresponding weak formulation and interface conditions, which are considered separately in Section 3.6.

3.1. *Original equations and constitutive assumptions*

We consider creeping flow, for which inertial acceleration is negligible relative to the pressure, viscous and body forces. The conservation of momentum equation therefore expresses an instantaneous force balance,

$$-\nabla p + \nabla \cdot \boldsymbol{\tau} + \mathbf{f}_b = \mathbf{0}, \tag{3.1}$$

together with the anelastic mass-conservation equation

$$\nabla \cdot (\rho_0 \mathbf{u}) = 0. \tag{3.2}$$

Here p is the pressure associated with the flow, $\boldsymbol{\tau}$ is the deviatoric stress, $\mathbf{u}$ is the physical velocity, and $\mathbf{f}_b$ is the physical body force per unit volume. The reference density entering the anelastic liquid approximation is denoted by $\rho_0(\mathbf{x})$.

We adopt the traceless Newtonian deviatoric stress

$$\boldsymbol{\tau} = \eta\, \mathsf{D}(\mathbf{u}), \tag{3.3}$$

where

$$\mathsf{D}(\mathbf{u}) = \nabla\mathbf{u} + (\nabla\mathbf{u})^{\mathsf{T}} - \frac{2}{3}\,(\nabla \cdot \mathbf{u})\,\mathbf{I}. \tag{3.4}$$

No independent bulk viscosity contribution is included (Landau & Lifshitz 1987).

The equations below are written in coordinate independent tensor notation. In Cartesian coordinates, the gradient convention is

$$(\nabla \mathbf{u})_{ij} = \frac{\partial u_i}{\partial x_j}.$$

In curvilinear coordinates, the same expressions must be interpreted using the corresponding covariant derivatives.

3.2. *Transformed constitutive relation*

We recall the definitions

$$\Lambda = \ln\left(\frac{\eta}{\eta_0}\right), \qquad \boldsymbol{\xi} = \nabla\Lambda, \qquad \mathbf{v} = \frac{\eta}{\eta_0}\mathbf{u}. \tag{3.5}$$

The physical velocity is therefore

$$\mathbf{u} = \frac{\eta_0}{\eta}\mathbf{v} = e^{-\Lambda}\mathbf{v}. \tag{3.6}$$

For two vectors $\mathbf{a}$ and $\mathbf{b}$, we denote their tensor product by $\mathbf{a}\otimes\mathbf{b}$, with Cartesian components

$$(\mathbf{a}\otimes\mathbf{b})_{ij} = a_i b_j. \tag{3.7}$$

Equivalently, its action on an arbitrary vector $\mathbf{c}$ is

$$(\mathbf{a}\otimes\mathbf{b})\,\mathbf{c} = \mathbf{a}\,(\mathbf{b}\cdot\mathbf{c})\,. \tag{3.8}$$

Using the gradient convention

$$(\nabla \mathbf{u})_{ij} = \frac{\partial u_i}{\partial x_j},$$

we differentiate Eq. (3.6) component by component:

$$\begin{aligned} \frac{\partial u_i}{\partial x_j} &= \frac{\partial}{\partial x_j}\left(e^{-\Lambda}v_i\right) \\ &= e^{-\Lambda}\left(\frac{\partial v_i}{\partial x_j} - v_i\frac{\partial \Lambda}{\partial x_j}\right). \end{aligned} \tag{3.9}$$

The logarithmic viscosity gradient appears because the spatial derivative of the reciprocal viscosity factor in Eq. (3.6) is

$$\nabla\left(\frac{1}{\eta}\right) = -\frac{1}{\eta}\nabla\ln\eta.$$

Thus $\boldsymbol{\xi}$ emerges directly from the velocity renormalization. In tensor notation, we write (3.9) as

$$\begin{aligned} \nabla\mathbf{u} &= \nabla\left(e^{-\Lambda}\mathbf{v}\right) \\ &= e^{-\Lambda}\left(\nabla\mathbf{v} - \mathbf{v}\otimes\boldsymbol{\xi}\right). \end{aligned} \tag{3.10}$$

Its transpose is

$$(\nabla\mathbf{u})^{\mathsf{T}} = e^{-\Lambda}\left[(\nabla\mathbf{v})^{\mathsf{T}} - \boldsymbol{\xi}\otimes\mathbf{v}\right], \tag{3.11}$$

and its trace is

$$\nabla\cdot\mathbf{u} = e^{-\Lambda}\left(\nabla\cdot\mathbf{v} - \mathbf{v}\cdot\boldsymbol{\xi}\right). \tag{3.12}$$

It is useful to define the symmetric traceless tensor

$$\mathsf{B}(\mathbf{v},\boldsymbol{\xi}) = \mathbf{v}\otimes\boldsymbol{\xi} + \boldsymbol{\xi}\otimes\mathbf{v} - \frac{2}{3}\,(\mathbf{v}\cdot\boldsymbol{\xi})\,\mathbf{I}. \tag{3.13}$$

Closely related component-wise couplings between viscosity-scaled velocity and logarithmic-viscosity gradients appear in earlier spherical spectral formulations (e.g. Zhang & Christensen 1993; Čadek & Fleitout 2003). The form introduced here collects the viscosity-dependent part of the transformed constitutive law into the single coordinate-independent symmetric, traceless tensor $\mathsf{B}(\mathbf{v},\boldsymbol{\xi})$. Substitution of Eqs. (3.10)–(3.12) into Eq. (3.4) gives

$$\mathsf{D}(\mathbf{u}) = e^{-\Lambda}\left[\mathsf{D}(\mathbf{v}) - \mathsf{B}(\mathbf{v},\boldsymbol{\xi})\right]. \tag{3.14}$$

Because $\eta = \eta_0 e^{\Lambda}$, the exponential factors cancel in the deviatoric stress:

$$\boxed{\boldsymbol{\tau} = \eta_0\left[\mathsf{D}(\mathbf{v}) - \mathsf{B}(\mathbf{v},\boldsymbol{\xi})\right].} \tag{3.15}$$

3.3. *Transformed mass conservation*

The conservation of mass equation must be transformed together with the momentum conservation equation. Substituting $\mathbf{u} = e^{-\Lambda}\mathbf{v}$ into Eq. (3.2) gives

$$\begin{aligned} 0 &= \nabla\cdot\left(\rho_0 e^{-\Lambda}\mathbf{v}\right) \\ &= e^{-\Lambda}\left[\nabla\cdot(\rho_0\mathbf{v}) - \rho_0\mathbf{v}\cdot\nabla\Lambda\right]. \end{aligned} \tag{3.16}$$

Since $e^{-\Lambda} > 0$, the transformed mass-conservation equation is

$$\boxed{\nabla\cdot(\rho_0\mathbf{v}) = \rho_0\mathbf{v}\cdot\boldsymbol{\xi}.} \tag{3.17}$$

Spatial viscosity variation therefore changes both the constitutive stress-strain-rate relation and the mass conservation constraint.

3.4. *Transformed momentum equation*

Substitution of Eq. (3.15) into the creeping-flow momentum balance gives

$$-\nabla p + \eta_0\nabla\cdot\mathsf{D}(\mathbf{v}) - \eta_0\nabla\cdot\mathsf{B}(\mathbf{v},\boldsymbol{\xi}) + \mathbf{f}_b = \mathbf{0}. \tag{3.18}$$

This form displays the instantaneous balance among pressure, viscous and body forces. Rearranging it so that the constant-viscosity Stokes operator remains on the left gives

$$\boxed{-\nabla p + \eta_0\nabla\cdot\mathsf{D}(\mathbf{v}) = \eta_0\nabla\cdot\mathsf{B}(\mathbf{v},\boldsymbol{\xi}) - \mathbf{f}_b.} \tag{3.19}$$

Equation (3.19) separates the chosen constant-viscosity Stokes operator, in the left-hand side, from the terms that describe spatial changes in viscosity and the body force, which are grouped together on the right-hand side. For a prescribed viscosity field, $\nabla\cdot\mathsf{B}(\mathbf{v},\boldsymbol{\xi})$ depends linearly on $\mathbf{v}$. In an iterative approach to solving (3.19), this term is evaluated from the current estimate of the renormalized velocity and acts computationally as an effective load.

For smooth viscosity fields, the tensor divergence may be expanded. In Cartesian components,

$$B_{ij} = v_i\xi_j + \xi_i v_j - \frac{2}{3}\,(v_k\xi_k)\,\delta_{ij}. \tag{3.20}$$

Applying the product rule gives

$$\frac{\partial B_{ij}}{\partial x_j} = v_i \frac{\partial \xi_j}{\partial x_j} + \xi_i \frac{\partial v_j}{\partial x_j} + \xi_j \frac{\partial v_i}{\partial x_j} + v_j \frac{\partial \xi_i}{\partial x_j} - \frac{2}{3}\frac{\partial}{\partial x_i}(v_k \xi_k)\,. \tag{3.21}$$

In vector notation this becomes

$$\begin{aligned}\nabla\cdot \mathsf{B}(\mathbf{v},\boldsymbol{\xi}) &= \mathbf{v}\,(\nabla\cdot\boldsymbol{\xi}) + (\nabla\cdot\mathbf{v})\,\boldsymbol{\xi} \\ &\quad + (\boldsymbol{\xi}\cdot\nabla)\,\mathbf{v} + (\mathbf{v}\cdot\nabla)\,\boldsymbol{\xi} - \frac{2}{3}\nabla\,(\mathbf{v}\cdot\boldsymbol{\xi})\,.\end{aligned} \tag{3.22}$$

The standard identity

$$\begin{aligned}\nabla\,(\mathbf{v}\cdot\boldsymbol{\xi}) &= (\mathbf{v}\cdot\nabla)\,\boldsymbol{\xi} + (\boldsymbol{\xi}\cdot\nabla)\,\mathbf{v} \\ &\quad + \mathbf{v}\times(\nabla\times\boldsymbol{\xi}) + \boldsymbol{\xi}\times(\nabla\times\mathbf{v})\end{aligned} \tag{3.23}$$

now provides the required simplification. Since $\boldsymbol{\xi} = \nabla\Lambda$,

$$\nabla\times\boldsymbol{\xi} = \mathbf{0}. \tag{3.24}$$

It follows that

$$\begin{aligned}(\boldsymbol{\xi}\cdot\nabla)\,\mathbf{v} + (\mathbf{v}\cdot\nabla)\,\boldsymbol{\xi} &= \nabla\,(\mathbf{v}\cdot\boldsymbol{\xi}) - \boldsymbol{\xi}\times(\nabla\times\mathbf{v}) \\ &= \nabla\,(\mathbf{v}\cdot\boldsymbol{\xi}) + (\nabla\times\mathbf{v})\times\boldsymbol{\xi}.\end{aligned} \tag{3.25}$$

Substitution into Eq. (3.22) yields

$$\boxed{\begin{aligned}\nabla\cdot \mathsf{B}(\mathbf{v},\boldsymbol{\xi}) &= \mathbf{v}\,(\nabla\cdot\boldsymbol{\xi}) + (\nabla\cdot\mathbf{v})\,\boldsymbol{\xi} \\ &\quad + \frac{1}{3}\nabla\,(\mathbf{v}\cdot\boldsymbol{\xi}) + (\nabla\times\mathbf{v})\times\boldsymbol{\xi}.\end{aligned}} \tag{3.26}$$

The reference operator can also be expanded:

$$\nabla\cdot \mathsf{D}(\mathbf{v}) = \nabla^2\mathbf{v} + \frac{1}{3}\nabla\,(\nabla\cdot\mathbf{v})\,. \tag{3.27}$$

Consequently, the expanded momentum-conservation equation is

$$\begin{aligned}-\nabla p + \eta_0\nabla^2\mathbf{v} + \frac{\eta_0}{3}\nabla\,(\nabla\cdot\mathbf{v}) = \eta_0\Big[&\mathbf{v}\,(\nabla\cdot\boldsymbol{\xi}) + (\nabla\cdot\mathbf{v})\,\boldsymbol{\xi} \\ &+ \frac{1}{3}\nabla\,(\mathbf{v}\cdot\boldsymbol{\xi}) + (\nabla\times\mathbf{v})\times\boldsymbol{\xi}\Big] - \mathbf{f}_b.\end{aligned} \tag{3.28}$$

Because

$$\nabla\cdot\boldsymbol{\xi} = \nabla^2\Lambda, \tag{3.29}$$

the fully expanded form of the momentum equation contains second spatial derivatives of logarithmic viscosity. The compact expression

$$\nabla\cdot \mathsf{B}(\mathbf{v},\boldsymbol{\xi})$$

does not remove those derivatives if it is evaluated pointwise: expanding this divergence again produces $\nabla\cdot\boldsymbol{\xi} = \nabla^2\Lambda$. Its advantage appears when the momentum-conservation equation is written in weak form.

To see this, let $\mathbf{w}$ be a sufficiently regular vector test function. Multiplying the contribution of viscous body force by $\mathbf{w}$, integrating over the fluid domain Ω, and applying the divergence theorem gives

$$\int_{\Omega} \mathbf{w} \cdot \nabla \cdot \mathsf{B}(\mathbf{v}, \boldsymbol{\xi})\, \mathrm{d}V = -\int_{\Omega} \nabla \mathbf{w} : \mathsf{B}(\mathbf{v}, \boldsymbol{\xi})\, \mathrm{d}V + \int_{\partial\Omega} \mathbf{w} \cdot \mathsf{B}(\mathbf{v}, \boldsymbol{\xi})\mathbf{n}\, \mathrm{d}S. \tag{3.30}$$

Here $\mathbf{n}$ is the outward unit normal to the boundary $\partial\Omega$, and the double contraction of two second-order tensors is defined by

$$\mathsf{A} : \mathsf{C} = A_{ij}C_{ij}.$$

After this integration by parts, the volume integral contains $\mathsf{B}(\mathbf{v}, \boldsymbol{\xi})$ itself rather than its divergence. It therefore requires only the first spatial derivative

$$\boldsymbol{\xi} = \nabla\Lambda,$$

and does not require the explicit numerical evaluation of $\nabla^2\Lambda$. The boundary integral must be retained or combined consistently with the transformed traction boundary condition.

Additionally, for any control volume Ω_c, the divergence theorem gives

$$\int_{\Omega_c} \nabla \cdot \mathsf{B}(\mathbf{v}, \boldsymbol{\xi})\, \mathrm{d}V = \int_{\partial\Omega_c} \mathsf{B}(\mathbf{v}, \boldsymbol{\xi})\mathbf{n}_c\, \mathrm{d}S, \tag{3.31}$$

where $\mathbf{n}_c$ is the outward unit normal to the boundary of the control volume. The volume integral on the left is an effective viscous force acting on that volume, while the surface integral on the right expresses the same force in terms of the effective traction across its boundary.

Applied separately to numerical control volumes, expression (3.31) provides the basis of a finite-volume discretization. The divergence is then evaluated from fluxes of $\mathsf{B}(\mathbf{v}, \boldsymbol{\xi})$ across cell faces. Since B depends on $\boldsymbol{\xi} = \nabla\Lambda$, but not explicitly on $\nabla^2\Lambda$, this procedure avoids the direct numerical evaluation of second derivatives of logarithmic viscosity.

Equation (3.19) is therefore the natural starting point for a weak discretization, especially when the viscosity varies rapidly across a thin but numerically resolved transition. If the viscosity is genuinely discontinuous, the differential equations are instead applied separately within each smooth subdomain, and the solutions are connected by the appropriate velocity and traction matching conditions at the intervening interfaces.

3.5. *Decomposition about a reference viscosity field*

The constant value η_0 fixes the overall normalization, but the operator may also retain a chosen spatially varying reference field, for example a reference viscosity that varies only in one dimension, typically varying with depth or, in the case of planetary interiors, varying with radius. We write

$$\Lambda = \Lambda_{\mathrm{ref}} + \delta\Lambda, \qquad \boldsymbol{\xi} = \boldsymbol{\xi}_{\mathrm{ref}} + \delta\boldsymbol{\xi}, \tag{3.32}$$

where

$$\boldsymbol{\xi}_{\mathrm{ref}} = \nabla\Lambda_{\mathrm{ref}}, \qquad \delta\boldsymbol{\xi} = \nabla\delta\Lambda. \tag{3.33}$$

Equivalently,

$$\eta_{\mathrm{ref}} = \eta_0 e^{\Lambda_{\mathrm{ref}}}, \qquad \eta = \eta_{\mathrm{ref}} e^{\delta\Lambda}. \tag{3.34}$$

Since B is linear in its second argument,

$$\mathsf{B}(\mathbf{v}, \boldsymbol{\xi}) = \mathsf{B}(\mathbf{v}, \boldsymbol{\xi}_{\mathrm{ref}}) + \mathsf{B}(\mathbf{v}, \delta\boldsymbol{\xi}). \tag{3.35}$$

The exact momentum-conservation equation can therefore be written as

$$-\nabla p + \eta_0 \nabla \cdot \left[\mathsf{D}(\mathbf{v}) - \mathsf{B}(\mathbf{v}, \boldsymbol{\xi}_{\mathrm{ref}})\right] = \eta_0 \nabla \cdot \mathsf{B}(\mathbf{v}, \delta\boldsymbol{\xi}) - \mathbf{f}_b. \tag{3.36}$$

The mass-conservation equation becomes

$$\nabla \cdot (\rho_0 \mathbf{v}) - \rho_0 \mathbf{v} \cdot \boldsymbol{\xi}_{\mathrm{ref}} = \rho_0 \mathbf{v} \cdot \delta\boldsymbol{\xi}. \tag{3.37}$$

Several useful choices follow from this exact decomposition.

For a constant (isoviscous) reference,

$$\Lambda_{\mathrm{ref}} = 0, \qquad \boldsymbol{\xi}_{\mathrm{ref}} = \mathbf{0},$$

all spatial viscosity variation appears in (3.36)–(3.37) on the right hand side. This is the form used in the numerical calculations presented in this paper.

For a one-dimensional, radially-varying reference relevant to planetary interiors,

$$\Lambda_{\mathrm{ref}} = \Lambda_0(r),$$

the radial viscosity structure remains within the reference operator, while departures from the radial profile enter through $\delta\Lambda$. This is the natural continuation of the radial formulation of Forte (2000) and of later spherical treatments of lateral viscosity variation (Čadek & Fleitout 2003; Rogozhina 2008).

A smooth reference field of another chosen form may also be retained in the operator. The decomposition remains exact, although the numerical value of any particular choice must be assessed separately.

3.6. *Boundary conditions and limiting cases*

The change of velocity variable must also be applied to the boundary conditions. For a prescribed physical velocity $\mathbf{u} = \mathbf{u}_b$,

$$\mathbf{v} = \frac{\eta}{\eta_0} \mathbf{u}_b. \tag{3.38}$$

In particular, because $\eta/\eta_0 \neq 0$,

$$\mathbf{u} = \mathbf{0} \quad \Longleftrightarrow \quad \mathbf{v} = \mathbf{0}, \tag{3.39}$$

and,

$$\mathbf{u} \cdot \mathbf{n} = 0 \quad \Longleftrightarrow \quad \mathbf{v} \cdot \mathbf{n} = 0. \tag{3.40}$$

For an impermeable boundary, the normal velocity vanishes at the boundary,

$$\mathbf{v} \cdot \mathbf{n} = 0. \tag{3.41}$$

A prescribed boundary traction $\mathbf{t}_b$ becomes

$$\left\{-p\mathbf{I} + \eta_0 \left[\mathsf{D}(\mathbf{v}) - \mathsf{B}(\mathbf{v}, \boldsymbol{\xi})\right]\right\} \mathbf{n} = \mathbf{t}_b. \tag{3.42}$$

We define the projection onto the plane tangent to the boundary by

$$\mathsf{P}_t = \mathbf{I} - \mathbf{n} \otimes \mathbf{n}, \tag{3.43}$$

where $\mathbf{n}$ is the outward unit normal and $\mathbf{I}$ is the identity tensor. For any vector $\mathbf{a}$,

$$\mathsf{P}_t \mathbf{a} = \mathbf{a} - (\mathbf{a} \cdot \mathbf{n})\, \mathbf{n}, \tag{3.44}$$

so that $\mathsf{P}_t \mathbf{a}$ is the component of $\mathbf{a}$ tangent to the boundary.

For a free-slip boundary, the vanishing of tangential traction can therefore be written in vector form as

$$(\mathbf{I} - \mathbf{n} \otimes \mathbf{n}) \left[\mathsf{D}(\mathbf{v}) - \mathsf{B}(\mathbf{v}, \boldsymbol{\xi})\right] \mathbf{n} = \mathbf{0}. \tag{3.45}$$

Using the impermeability condition (3.41), this becomes

$$(\mathbf{I} - \mathbf{n} \otimes \mathbf{n}) \left[\nabla \mathbf{v} + (\nabla \mathbf{v})^{\mathsf{T}}\right] \mathbf{n} = (\boldsymbol{\xi} \cdot \mathbf{n})\, \mathbf{v}. \tag{3.46}$$

Thus the normal gradient of logarithmic viscosity contributes explicitly to the tangential boundary condition for the renormalized velocity. The conventional constant viscosity form is recovered when $\boldsymbol{\xi} \cdot \mathbf{n} = 0$. Thus the ordinary constant viscosity free slip condition cannot simply be imposed on $\mathbf{v}$ when $\boldsymbol{\xi} \cdot \mathbf{n} \neq \mathbf{0}$.

Suppose that an internal interface Γ separates two subdomains in which ρ_0 and η are individually smooth, but may have finite jumps across Γ. Let $\mathbf{n}$ denote the unit normal directed from the minus side to the plus side, and let $[\![\cdot]\!]$ denote the corresponding jump.

Care is required when the reference density is discontinuous (Forte 2007). For a fixed interface, the anelastic mass-conservation equation

$$\nabla \cdot (\rho_0 \mathbf{u}) = 0$$

implies continuity of normal mass flux,

$$[\![\rho_0\, \mathbf{u} \cdot \mathbf{n}]\!] = 0, \tag{3.47}$$

rather than continuity of the normal velocity itself. If $\rho_0^+ \neq \rho_0^-$ and material crosses the interface, then

$$\rho_0^+\, \mathbf{u}^+ \cdot \mathbf{n} = \rho_0^-\, \mathbf{u}^- \cdot \mathbf{n},$$

so the normal component of $\mathbf{u}$ is generally discontinuous.

For a mechanically bonded interface with no tangential slip, the tangential velocity remains continuous:

$$[\![\mathbf{P}_t \mathbf{u}]\!] = \mathbf{0}, \qquad \mathbf{P}_t = \mathbf{I} - \mathbf{n} \otimes \mathbf{n}. \tag{3.48}$$

In the absence of a singular interfacial force or surface tension, the physical traction is also continuous:

$$[\![\boldsymbol{\sigma} \mathbf{n}]\!] = \mathbf{0}, \qquad \boldsymbol{\sigma} = -p\mathbf{I} + \boldsymbol{\tau}. \tag{3.49}$$

Using

$$\mathbf{u} = \frac{\eta_0}{\eta} \mathbf{v},$$

the fixed-interface mass-flux and tangential-velocity conditions become

$$\left[\!\!\left[\rho_0 \frac{\eta_0}{\eta} \mathbf{v} \cdot \mathbf{n}\right]\!\!\right] = 0, \tag{3.50}$$

and

$$\left[\!\!\left[\frac{\eta_0}{\eta} \mathbf{P}_t \mathbf{v}\right]\!\!\right] = \mathbf{0}. \tag{3.51}$$

At a true viscosity discontinuity, $\boldsymbol{\xi} = \nabla \Lambda$ contains an interfacial distribution. The smooth-field expression for the transformed stress is therefore applied separately within each subdomain. Denoting one-sided limits by superscripts + and −, we define

$$\boldsymbol{\sigma}^\pm = -p^\pm \mathbf{I} + \eta_0 \left[\mathsf{D}(\mathbf{v}^\pm) - \mathsf{B}\left(\mathbf{v}^\pm, \boldsymbol{\xi}^\pm\right)\right], \qquad \boldsymbol{\xi}^\pm = \nabla \Lambda^\pm. \tag{3.52}$$

Traction continuity is then imposed through the one-sided stresses:

$$[\![\boldsymbol{\sigma}\mathbf{n}]\!] = \boldsymbol{\sigma}^{+}\mathbf{n} - \boldsymbol{\sigma}^{-}\mathbf{n} = \mathbf{0}. \tag{3.53}$$

The viscosity jump is thus represented by the interface conditions, rather than by evaluating the singular part of $\nabla\Lambda$ inside $\mathsf{B}(\mathbf{v},\boldsymbol{\xi})$.

For a spatially constant viscosity,

$$\boldsymbol{\xi} = \mathbf{0},$$

and the transformed equations reduce to

$$-\nabla p + \eta_0 \nabla \cdot \mathsf{D}(\mathbf{v}) = -\mathbf{f}_b, \qquad \nabla \cdot (\rho_0 \mathbf{v}) = 0. \tag{3.54}$$

Only when ρ_0 is also constant does the second equation become

$$\nabla \cdot \mathbf{v} = 0.$$

In that Boussinesq limit,

$$\nabla \cdot \mathsf{D}(\mathbf{v}) = \nabla^2 \mathbf{v}.$$

The absence of lateral viscosity variation is not the same as the isoviscous limit. A viscosity field that depends only on radius still has nonzero $\boldsymbol{\xi} = (d\Lambda/dr)\widehat{\mathbf{r}}$ and therefore retains viscosity gradient terms.

3.7. *Hydrostatic reference state, buoyancy and self gravity*

For applications to planetary interiors, the body force is gravitational. The body force per unit volume is therefore

$$\mathbf{f}_b = \rho \mathbf{g} = \rho \nabla \phi. \tag{3.55}$$

We use the gravitational potential convention common in geophysical and geodynamic studies:

$$\mathbf{g} = \nabla \phi, \qquad \nabla^2 \phi = -4\pi G \rho. \tag{3.56}$$

With this convention, the gravitational acceleration in a radial reference state is

$$\nabla \phi_0 = -g_0 \widehat{\mathbf{r}}, \qquad g_0 > 0. \tag{3.57}$$

The total momentum-conservation equation is

$$-\nabla p + \nabla \cdot \boldsymbol{\tau} + \rho \nabla \phi = \mathbf{0}. \tag{3.58}$$

We introduce perturbations relative to a hydrostatic reference state:

$$p = p_0 + \delta p, \qquad \rho = \rho_0 + \delta \rho, \qquad \phi = \phi_0 + \delta \phi. \tag{3.59}$$

The reference state satisfies the condition of hydrostatic equilibrium

$$-\nabla p_0 + \rho_0 \nabla \phi_0 = \mathbf{0}. \tag{3.60}$$

Substituting (3.59) into (3.58), retaining terms that are first order in δp, $\delta \rho$ and $\delta \phi$, and neglecting products such as $\delta \rho \, \nabla \delta \phi$, and subtracting (3.60) gives

$$-\nabla \delta p + \nabla \cdot \boldsymbol{\tau} = \delta \rho \, g_0 \widehat{\mathbf{r}} - \rho_0 \nabla \delta \phi. \tag{3.61}$$

Using Eq. (3.15), the final transformed momentum-conservation equation relative to a hydrostatic background is

$$\boxed{-\nabla \delta p + \eta_0 \nabla \cdot \mathsf{D}(\mathbf{v}) = \eta_0 \nabla \cdot \mathsf{B}(\mathbf{v},\boldsymbol{\xi}) + \delta \rho \, g_0 \widehat{\mathbf{r}} - \rho_0 \nabla \delta \phi.} \tag{3.62}$$

It is accompanied by

$$\boxed{\nabla \cdot (\rho_0 \mathbf{v}) = \rho_0 \mathbf{v} \cdot \boldsymbol{\xi},} \tag{3.63}$$

and by the perturbation of Poisson's equation,

$$\nabla^2 \delta\phi = -4\pi G\, \delta\rho. \tag{3.64}$$

The gravitational potential and its normal derivative are continuous across an internal interface without a singular surface mass. At the outer boundary, $\delta\phi$ must be matched to an exterior harmonic potential that decays at infinity. When self gravity is not included, the term $-\rho_0 \nabla\delta\phi$ and Eq. (3.64) are omitted.

Equations (3.62), (3.63) and (3.64), together with the transformed boundary conditions, define the logarithmic viscosity formulation of the Stokes equations of motion that are relevant to planetary interiors. The spatial viscosity terms may be evaluated using a fixed reference operator, but they remain part of the exact Stokes problem and depend linearly on the renormalized velocity when viscosity is prescribed.

3.8. *Spectral treatment in three-dimensional spherical-shell geometry*

We now specialize the transformed equations to a three-dimensional spherical shell, where the constant-viscosity reference problem admits a natural vector-spherical-harmonic representation and exact solutions expressed by closed-form Green functions (Forte & Peltier 1987, 1994). This geometry is particularly useful for laterally varying viscosity because the viscosity field can couple spherical-harmonic components that are independent in a spherically symmetric reference model and can couple the poloidal and toroidal parts of the velocity field (Forte & Peltier 1994). We therefore develop here the spectral form of the fixed reference operator, later used in the spherical calculation of Section 4.3.

Let the shell occupy $b \le r \le a$. The reference Stokes-flow Green operator used below has constant viscosity η_0 and constant reference density ρ_0, with incompressible physical velocity. Under these Boussinesq assumptions, the self-gravitational perturbation enters the momentum equation as the pure gradient

$$\rho_0 \nabla\delta\phi = \nabla(\rho_0 \delta\phi)\,,$$

and may therefore be absorbed into the dynamic pressure; it does not alter the viscous velocity field (Forte & Peltier 1987). Self-gravity nevertheless contributes to the pressure and therefore to dynamic topography and the non-hydrostatic geoid anomalies.

We write either the renormalized or the physical velocity in vector spherical harmonics as

$$\mathbf{w}(r,\theta,\phi) = \sum_{\ell m} \left[U^{(w)}_{\ell m}(r) Y_{\ell m} \hat{\boldsymbol{r}} + V^{(w)}_{\ell m}(r) \nabla_1 Y_{\ell m} + W^{(w)}_{\ell m}(r) \hat{\boldsymbol{r}} \times \nabla_1 Y_{\ell m} \right], \qquad \mathbf{w} \in \{\mathbf{v}, \mathbf{u}\}, \tag{3.65}$$

where ∇_1 is the dimensionless surface gradient on the unit sphere. With this convention,

$$\nabla = \hat{\boldsymbol{r}} \frac{\partial}{\partial r} + \frac{1}{r} \nabla_1. \tag{3.66}$$

Representation (3.65) belongs to the classical theory of vector fields in spherical geometry. Following the dynamo formulation of Backus (1958) and its later development in terms of surface operators and the Mie poloidal–toroidal representation (Backus 1967, 1986), Forte & Peltier (1987, 1994) employed the dimensionless angular operator

$$\boldsymbol{\Lambda}_1 \equiv \boldsymbol{r} \times \nabla = \hat{\boldsymbol{r}} \times \nabla_1. \tag{3.67}$$

The subscript 1 denotes the unit-sphere angular operator and distinguishes it from the scalar logarithmic-viscosity field $\Lambda = \ln(\eta/\eta_0)$. Acting on a scalar spherical harmonic,

$$\boldsymbol{\Lambda}_1 Y_{\ell m} = \hat{\boldsymbol{r}} \times \nabla_1 Y_{\ell m}, \qquad \nabla_1 Y_{\ell m} = -\hat{\boldsymbol{r}} \times \boldsymbol{\Lambda}_1 Y_{\ell m}. \tag{3.68}$$

The $V_{\ell m}$ and $W_{\ell m}$ terms in Eq. (3.65) are therefore mutually orthogonal tangential basis fields. The first is spheroidal and the second toroidal. Together, $U_{\ell m}$ and $V_{\ell m}$ describe the radial and horizontal components of the spheroidal field, while $W_{\ell m}$ independently describes the toroidal field.

For a solenoidal velocity, the spheroidal field reduces to the classical poloidal field. In the Backus representation it may be written, together with the toroidal field, as

$$\mathbf{u} = \nabla \times (\boldsymbol{\Lambda}_1 \mathcal{P}) + \boldsymbol{\Lambda}_1 \mathcal{T}, \tag{3.69}$$

where $\mathcal{P}$ and $\mathcal{T}$ are poloidal and toroidal generating scalars. Equivalently, the two spheroidal coefficients of a solenoidal harmonic may be generated from a single radial poloidal scalar $P_{\ell m}$:

$$U^P_{\ell m} = \frac{\ell(\ell+1)}{r} P_{\ell m}, \qquad V^P_{\ell m} = \frac{\mathrm{d}P_{\ell m}}{\mathrm{d}r} + \frac{P_{\ell m}}{r}. \tag{3.70}$$

The renormalized velocity requires an additional spheroidal degree of freedom. For constant ρ_0, Eq. (3.17) becomes

$$\nabla \cdot \mathbf{v} = \mathbf{v} \cdot \boldsymbol{\xi}, \qquad \boldsymbol{\xi} = \nabla \Lambda, \tag{3.71}$$

so $\mathbf{v}$ is not generally solenoidal even though the physical velocity $\mathbf{u} = e^{-\Lambda}\mathbf{v}$ is. Consequently, $U^{(v)}_{\ell m}$ and $V^{(v)}_{\ell m}$ cannot in general be generated from a single poloidal scalar. The spherical reference inverse must therefore respond not only to a vector momentum source but also to the scalar source in the transformed mass equation.

To make this structure explicit, let $\mathbf{Q}_b$ denote the fixed physical momentum source. In the notation of Eq. (3.19), $\mathbf{Q}_b = -\mathbf{f}_b$; in the hydrostatic formulation of Eq. (3.62), it is the corresponding buoyancy and, when retained, self-gravity contribution. Define

$$\mathbf{q}_\eta[\mathbf{v}] = \eta_0 \nabla \cdot \mathsf{B}(\mathbf{v}, \boldsymbol{\xi}), \tag{3.72}$$

$$\mathbf{Q}[\mathbf{v}] = \mathbf{Q}_b + \mathbf{q}_\eta[\mathbf{v}], \tag{3.73}$$

$$s[\mathbf{v}] = \mathbf{v} \cdot \boldsymbol{\xi}. \tag{3.74}$$

The constant-reference problem may then be written

$$-\nabla p + \eta_0 \nabla \cdot \mathsf{D}(\mathbf{v}) = \mathbf{Q}[\mathbf{v}], \tag{3.75}$$

$$\nabla \cdot \mathbf{v} = s[\mathbf{v}]. \tag{3.76}$$

For prescribed viscosity, the viscosity-dependent parts of both sources are linear in $\mathbf{v}$. Equations (3.75) and (3.76) therefore constitute a self-consistent linear Stokes problem; the particular numerical realization used below is described in Section 4.3.

The effective momentum source is expanded in the same vector spherical-harmonic basis,

$$\mathbf{Q}(r,\theta,\phi) = \sum_{\ell m} \left[Q^R_{\ell m}(r) Y_{\ell m} \hat{\boldsymbol{r}} + Q^S_{\ell m}(r) \nabla_1 Y_{\ell m} + Q^T_{\ell m}(r) \hat{\boldsymbol{r}} \times \nabla_1 Y_{\ell m} \right], \tag{3.77}$$

while

$$s(r,\theta,\phi) = \sum_{\ell m} s_{\ell m}(r) Y_{\ell m}(\theta,\phi). \tag{3.78}$$

Writing

$$L = \ell(\ell + 1), \tag{3.79}$$

the transformed mass equation becomes

$$\frac{\mathrm{d}U^{(v)}_{\ell m}}{\mathrm{d}r} + \frac{2}{r}U^{(v)}_{\ell m} - \frac{L}{r}V^{(v)}_{\ell m} = s_{\ell m}. \tag{3.80}$$

This relation displays directly the additional spheroidal freedom introduced by velocity renormalization.

The transformed free-slip condition remains the general condition derived in Section 3.6. The closed-form Green operator used in the spherical calculation employs the important special case $\partial_r \Lambda = 0$ at both shell boundaries. Under this condition the transformed impermeable free-slip conditions reduce to the homogeneous reference conditions

$$U^{(v)}_{\ell m} = 0, \tag{3.81}$$

$$\frac{\mathrm{d}V^{(v)}_{\ell m}}{\mathrm{d}r} + \frac{U^{(v)}_{\ell m} - V^{(v)}_{\ell m}}{r} = 0, \tag{3.82}$$

$$\frac{\mathrm{d}W^{(v)}_{\ell m}}{\mathrm{d}r} - \frac{W^{(v)}_{\ell m}}{r} = 0, \tag{3.83}$$

at $r = b$ and $r = a$.

It is now useful to define the reference Stokes operator itself. For a prescribed source pair $(\mathbf{Q}, s)$,

$$\mathcal{L}_0 \begin{pmatrix} \mathbf{v} \\ p \end{pmatrix} = \begin{pmatrix} \mathbf{Q} \\ s \end{pmatrix}, \qquad \mathcal{L}_0 = \begin{pmatrix} \eta_0 \nabla \cdot \mathsf{D} & -\nabla \\ \nabla \cdot & 0 \end{pmatrix}, \tag{3.84}$$

subject to Eqs. (3.81)–(3.83). Once the arbitrary additive pressure constant and the degree-one rigid-rotation null space are fixed (Appendix A), the inverse exists on the admissible source space. This inverse corresponds to the Green solution operator (Appendix B), as shown here:

$$\mathcal{G}_0 \equiv \mathcal{L}_0^{-1}, \qquad \begin{pmatrix} \mathbf{v} \\ p \end{pmatrix} = \mathcal{G}_0 \begin{pmatrix} \mathbf{Q} \\ s \end{pmatrix}. \tag{3.85}$$

Linearity gives the useful decomposition

$$\mathcal{G}_0 \begin{pmatrix} \mathbf{Q} \\ s \end{pmatrix} = \mathcal{G}_0 \begin{pmatrix} \mathbf{Q} \\ 0 \end{pmatrix} + \mathcal{G}_0 \begin{pmatrix} 0 \\ s \end{pmatrix}. \tag{3.86}$$

The first term is the force-driven Stokes response and contains spheroidal (poloidal) and toroidal parts. The second is generated solely by the transformed mass source and is spheroidal.

The radial structure of these three responses follows from the scalar operator

$$\mathcal{D}_\ell f = \frac{\mathrm{d}^2 f}{\mathrm{d}r^2} + \frac{2}{r}\frac{\mathrm{d}f}{\mathrm{d}r} - \frac{L}{r^2} f. \tag{3.87}$$

For the force-driven spheroidal response, the solenoidal part is represented by a poloidal scalar $P^F_{\ell m}$. Following Forte & Peltier (1987), taking the curl of the spheroidal momentum equation eliminates pressure and gives

$$\eta_0 \mathcal{D}_\ell^2 P^F_{\ell m} = C_{\ell m}, \tag{3.88}$$

where

$$C_{\ell m} = \frac{1}{r}\left[\frac{\mathrm{d}}{\mathrm{d}r}\left(rQ^S_{\ell m}\right) - Q^R_{\ell m}\right]. \tag{3.89}$$

Impermeability and free slip become

$$P^F_{\ell m} = \frac{\mathrm{d}^2 P^F_{\ell m}}{\mathrm{d}r^2} = 0 \qquad \text{at } r = b, a, \tag{3.90}$$

and the force-driven velocity coefficients follow from Eq. (3.70). Expanding $p^F = \sum_{\ell m} p^F_{\ell m}(r) Y_{\ell m}$, the pressure coefficient is

$$p^F_{\ell m} = \eta_0 \frac{\mathrm{d}}{\mathrm{d}r}\left(r\mathcal{D}_\ell P^F_{\ell m}\right) - rQ^S_{\ell m}. \tag{3.91}$$

The force-driven toroidal response obeys the second-order equation

$$\eta_0 \mathcal{D}_\ell W^F_{\ell m} = Q^T_{\ell m}, \tag{3.92}$$

with the free-slip condition Eq. (3.83). Radial buoyancy has no direct toroidal projection for a spherically symmetric viscosity distribution (Forte 2007). Toroidal forcing generated by lateral viscosity must therefore enter through the viscosity-dependent momentum source. The degeneracy inherent in the degree-one toroidal null mode is treated in Appendix A.

The classical poloidal and toroidal momentum responses do not complete the transformed problem when $s_{\ell m} \neq 0$. For each scalar harmonic, the third Green response satisfies

$$-\nabla\left[p^M_{\ell m}(r)Y_{\ell m}\right] + \eta_0 \nabla\cdot \mathsf{D}\left(\mathbf{v}^M_{\ell m}\right) = \mathbf{0}, \tag{3.93}$$

$$\nabla\cdot\mathbf{v}^M_{\ell m} = s_{\ell m}(r) Y_{\ell m}. \tag{3.94}$$

This response is spheroidal. It may be constructed from a divergence-generating gradient field together with a divergence-free poloidal boundary correction, so that momentum conservation, the transformed mass equation, impermeability, and zero tangential traction are satisfied simultaneously. The complete harmonic coefficients are therefore

$$U^{(v)}_{\ell m} = U^F_{\ell m} + U^M_{\ell m}, \qquad V^{(v)}_{\ell m} = V^F_{\ell m} + V^M_{\ell m}, \qquad W^{(v)}_{\ell m} = W^F_{\ell m}. \tag{3.95}$$

This linear superposition of momentum-forced and mass-forced flow components follows directly from (3.86). The closed-form radial Green kernels for the force-driven poloidal response, the force-driven toroidal response, and the transformed-mass response are presented in Appendix B.

At an impermeable spherical surface, $U^{(u)}_{\ell m} = 0$, and the tangential physical velocity is completely described by $V^{(u)}_{\ell m}$ and $W^{(u)}_{\ell m}$. Following Forte & Peltier (1987), the corresponding two-scalar representation of surface flow kinematics is

$$D_{\ell m}(r) = -\frac{\ell(\ell+1)}{r} V^{(u)}_{\ell m}(r), \qquad R_{\ell m}(r) = -\frac{\ell(\ell+1)}{r} W^{(u)}_{\ell m}(r), \tag{3.96}$$

where $D = r^{-1}\nabla_1 \cdot \mathbf{u}_H$ is the horizontal divergence and $R = \hat{\boldsymbol{r}}\cdot\nabla\times\mathbf{u}$ is the radial vorticity. These two scalar fields isolate the poloidal and toroidal parts of the surface motion, respectively (Forte & Peltier 1987, 1994).

The reconstruction $\mathbf{u} = e^{-\Lambda}\mathbf{v}$ also has an important spectral consequence. Equation (3.12) gives the divergence of the physical velocity, while its curl is

$$\nabla\times\mathbf{u} = e^{-\Lambda}\left[\nabla\times\mathbf{v} - \nabla\Lambda\times\mathbf{v}\right]. \tag{3.97}$$

Thus physical reconstruction is a local scalar multiplication, whereas the poloidal–toroidal decomposition is a global differential operation. The two do not commute in general, so the poloidal–toroidal partition of the renormalized velocity need not be preserved after reconstruction of the physical velocity.

The same spectral representation also makes the allowed spherical-harmonic coupling pathways explicit. For a poloidal component of degree s coupled by a viscosity harmonic of degree L_η, the generalized spherical-harmonic selection rules of Forte & Peltier (1994) permit the poloidal degrees

$$|L_\eta - s|,\ |L_\eta - s| + 2, \dots, L_\eta + s, \tag{3.98}$$

and the toroidal degrees

$$|L_\eta - s| + 1,\ |L_\eta - s| + 3, \dots, L_\eta + s - 1. \tag{3.99}$$

These rules determine which harmonic channels are allowed by the angular coupling. Their direct application to the spherical-shell flow calculation is examined in Section 4.3.

In the isoviscous limit, $\boldsymbol{\xi} = \mathbf{0}$. The viscosity-induced momentum source and the transformed mass source then vanish, $\mathbf{v} = \mathbf{u}$, and the reference problem reduces to the familiar solenoidal poloidal–toroidal system. Radial buoyancy excites only poloidal flow; the only toroidal freedom is the arbitrary degree-one rigid-rotation null mode. Lateral viscosity variation breaks this simple spectral structure by generating both spheroidal and toroidal momentum sources together with the additional transformed-mass response.

4. Validation and Illustrative Applications

Sections 2 and 3 provide an exact reformulation of the variable-viscosity Stokes problem. We now test its numerical accuracy, convergence and robustness. We proceed by addressing three progressively more demanding modelling problems. We first investigate whether the transformed equations recover a velocity field that is known in advance. We then explore whether they reproduce a simple and transparent physical consequence of a large viscosity contrast. Finally, we carry the formulation into a spherical shell and examine the mode coupling that arises when a large lateral viscosity variation acts on a simple buoyancy forcing. The first two problems provide controlled numerical and physical tests. The third tests the formulation in spherical-shell geometry, reflecting its original motivation in the study of planetary mantle dynamics.

4.1. *Manufactured solution benchmark*

We begin with a manufactured solution in a two dimensional Cartesian domain. The purpose of this calculation is deliberately narrow. By prescribing a smooth velocity field and deriving the force required to sustain it, we obtain an exact solution of the variable-viscosity Stokes equations against which we test both the direct numerical solution of the original equations and the transformed formulation developed in Sections 2 and 3. The analytical velocity field is

$$\begin{aligned} e(x,y) &= A f(x) f'(y), \\ n(x,y) &= -A f'(x) f(y), \end{aligned} \tag{4.1}$$

with

$$f(x) = x^3(1-x)^3. \tag{4.2}$$

It follows directly that

$$\frac{\partial e}{\partial x} + \frac{\partial n}{\partial y} = 0, \tag{4.3}$$

so the prescribed field satisfies incompressibility exactly. For the prescription of $f(x)$ given above, it follows that

$$f(0) = f(1) = f'(0) = f'(1) = f''(0) = f''(1) = 0.$$

Consequently, the normal velocity vanishes on every boundary and the tangential viscous traction,

$$\tau_{xy} = A\eta\,[f(x)f''(y) - f''(x)f(y)]\,,$$

also vanishes there. The prescribed field therefore satisfies the impermeable free-slip boundary conditions exactly.

We set

$$p(x, y) = 0 \tag{4.4}$$

and derive the corresponding body force analytically. In this way the comparison isolates the viscous terms and their spatial variation rather than uncertainty in the forcing.

The viscosity is prescribed as

$$\eta(x, y) = \exp[-\gamma T(x, y)]\,, \tag{4.5}$$

where

$$T(x, y) = 4x(1 - x)\,4y(1 - y) \tag{4.6}$$

and

$$\gamma = \ln C. \tag{4.7}$$

The parameter C therefore sets the total viscosity contrast. The calculation spans four orders of magnitude in viscosity.

Figure 1 shows both η and $\ln\eta$. The comparison is useful because it makes visible the compression of a large multiplicative range in viscosity into the much gentler additive range of its logarithm.

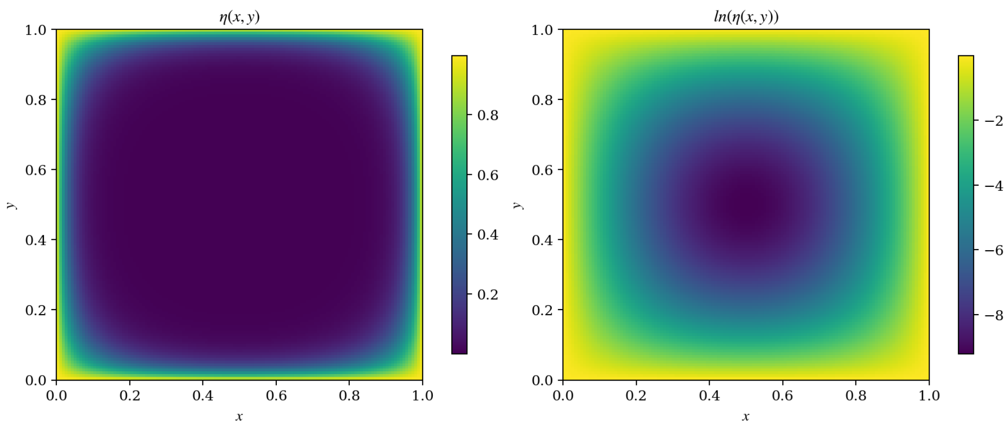

Figure 1. Prescribed viscosity in the manufactured solution benchmark. The left panel shows $\eta(x, y)$. The right panel shows $\ln\eta(x, y)$, the field whose gradient enters the transformed equations. The viscosity varies smoothly across four orders of magnitude. The two panels therefore also illustrate the compression of a large multiplicative viscosity range when it is represented in logarithmic form.

Figures 2 and 3 compare the exact velocity with the solutions obtained from the direct variable viscosity discretization and from the transformed formulation on a 128×128 grid. The upper rows show the fields themselves. The lower rows show the error of each numerical solution relative to the exact field and the difference between the two numerical solutions. The symbol E in the figure panels denotes the relative L_2 error.

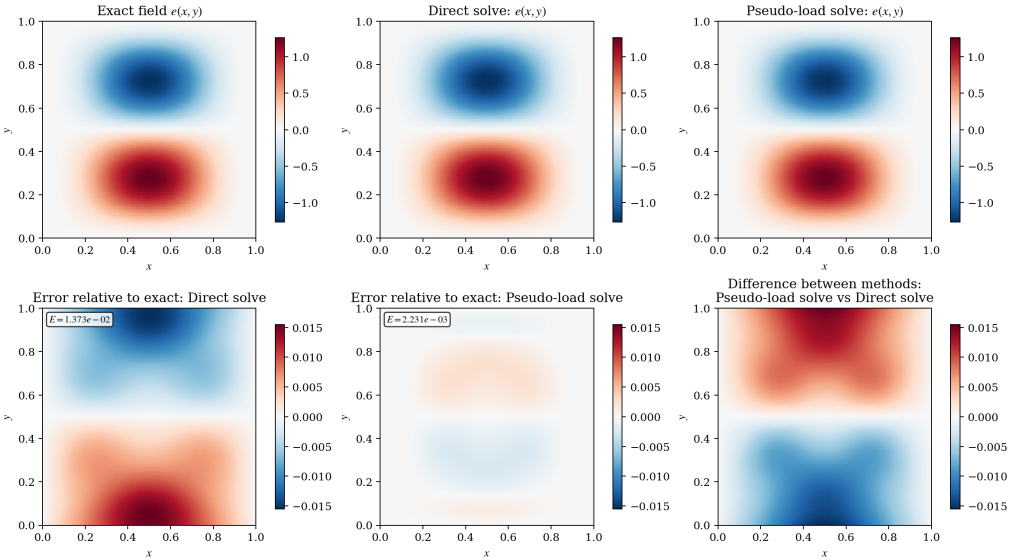

Figure 2. Manufactured solution benchmark for the velocity component $e(x, y)$ on a 128×128 grid. The upper row shows the exact field, the solution from the direct variable viscosity discretization, and the solution from the transformed formulation. The lower row shows the corresponding errors relative to the exact field and, at right, the difference between the two numerical solutions. The quantity E denotes the relative L_2 error.

Both formulations approach the manufactured solution as the grid is refined. For the particular pair of discretizations compared here, however, the transformed formulation has the smaller error at every tested resolution. The distinction is already apparent in Figs. 2 and 3, where the error fields remain smooth and coherent. It is quantified in Table 1. On the finest grid, the relative L_2 error is 1.373×10^{-2} for the direct discretization and 2.231×10^{-3} for the transformed solution. The reduction is about a factor of six. For this manufactured solution, the transformed formulation remains accurate across a viscosity contrast of 10^4 and yields substantially smaller numerical errors than the direct variable-viscosity discretization used for comparison.

At each iteration, the viscosity-dependent term $\eta_0 \nabla \cdot \mathsf{B}(\mathbf{v}, \boldsymbol{\xi})$ on the right-hand side of Eq. (3.19) is evaluated from the current estimate of $\mathbf{v}$, and the resulting constant-viscosity reference Stokes problem is solved again. At large viscosity contrasts, an under-relaxed fixed-point iteration provides more reliable convergence than an undamped update. We therefore write the update as

$$Z^{k+1} = (1 - \alpha) Z^k + \alpha \widetilde{Z}^{k+1}, \tag{4.8}$$

where Z^k is the current iterate, $\widetilde{Z}^{k+1}$ is the newly computed value before relaxation, and α is the relaxation parameter. For the manufactured solution test we use $\alpha = 0.2$, selected from a set of trial values. The relative change between successive iterates decreases monotonically in Fig. 4 and reaches the prescribed tolerance without an oscillatory phase. The convergence

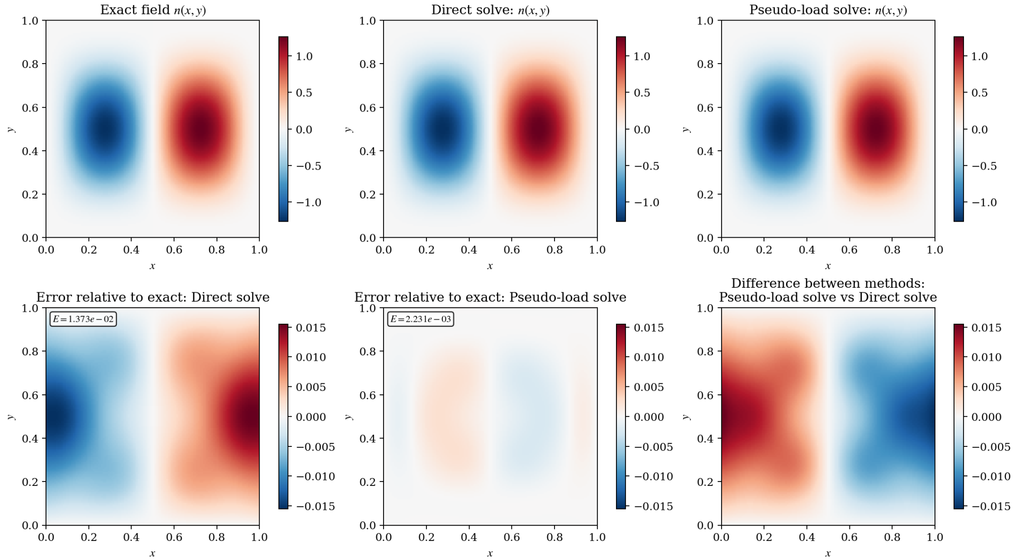

Figure 3. As in Fig. 2, but for the velocity component $n(x, y)$. The exact field and the two numerical solutions are shown above. Their errors and mutual difference are shown below. The close agreement of the transformed solution with the prescribed field is obtained while the viscosity varies by four orders of magnitude.

Table 1. Relative L_2 errors in the manufactured solution benchmark. Here $E_e^{(d)}$ and $E_n^{(d)}$ are the errors of the direct variable viscosity discretization, while $E_e^{(p)}$ and $E_n^{(p)}$ are those of the transformed formulation. All errors are measured against the exact manufactured solution. The uniform grid spacing is denoted by h.

Grid	h	$E_e^{(d)}$	$E_e^{(p)}$	$E_n^{(d)}$	$E_n^{(p)}$
16×16	6.250e-02	6.656e-01	1.467e-01	6.656e-01	1.467e-01
32×32	3.125e-02	2.045e-01	3.583e-02	2.045e-01	3.583e-02
64×64	1.562e-02	5.413e-02	8.923e-03	5.413e-02	8.923e-03
128×128	7.812e-03	1.373e-02	2.231e-03	1.373e-02	2.231e-03

history therefore validates the iterative procedure itself, showing that the numerical solution approaches the exact solution stably rather than merely agreeing with it at the final iteration.

4.2. *Two-region Cartesian benchmark*

The previous section verified the numerical implementation against a prescribed exact solution. We now turn to a complementary benchmark that tests the formulation in a problem with a sharp viscosity contrast and independently interpretable flow structure.

At low Reynolds number, the characteristic velocity generated by a fixed buoyancy force scales inversely with the surrounding viscosity. We use this simple fact to construct a two-region test. The Cartesian domain is divided at $x = 0.5$. The right half has viscosity $\eta_R = 1$, while the left half has viscosity η_L. Two identical negatively buoyant bodies are placed at the same depth, one on either side of the interface. Their density anomalies, sizes, and positions relative to the centre of each half are the same. Viscosity is thus the only intended distinction between their environments.

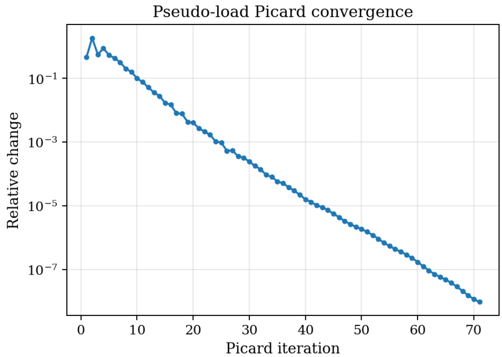

Figure 4. Convergence of the fixed point iteration for the manufactured solution benchmark. The ordinate is the relative change between successive iterates. With $\alpha = 0.2$, the change decreases monotonically until the stopping tolerance is reached. The calculation uses the same four order viscosity contrast as Figs. 1–3.

Figure 5 shows the viscosity field and the imposed density anomalies. Both are smoothed over finite distances. This choice keeps the numerical derivatives finite and avoids making the comparison sensitive to the particular grid representation of a discontinuous coefficient.

The expected behaviour is familiar from the classical Stokes-sinker problem. At negligible Reynolds number, the settling speed of a sphere of fixed size and density contrast is inversely proportional to the viscosity of the surrounding fluid. Our smoothed density anomalies are neither rigid spheres nor isolated bodies in an unbounded fluid, so the classical Stokes formula is not expected to apply quantitatively. It nevertheless provides a simple physical scaling against which the computed response can be interpreted.

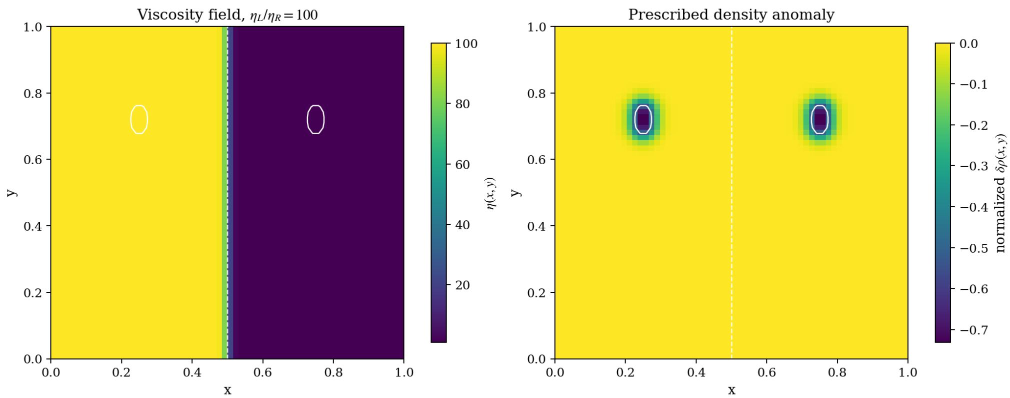

Figure 5. Geometry of the two region Cartesian benchmark on a 64×64 grid. The left panel shows the prescribed viscosity for $\eta_L/\eta_R = 100$. The more viscous material occupies the left half of the box. The right panel shows the two identical normalized density anomalies. The dashed line marks the centre of the viscosity transition and the white contours outline the buoyant bodies. The transition in viscosity and the edges of the density anomalies are smoothed over finite widths.

The response is shown in Fig. 6. When $\eta_L/\eta_R = 1$, symmetry is recovered. The two bodies sink at nearly the same speed and the surrounding circulation is mirrored across the centre of the box. When the left half is made one thousand times more viscous, that symmetry is broken in the expected way. Motion around the left body is strongly reduced, whereas the body in the reference viscosity half continues to drive a much larger flow.

The calculation therefore captures not only a change in a scalar sinking speed, but also the associated redistribution of the surrounding Stokes flow.

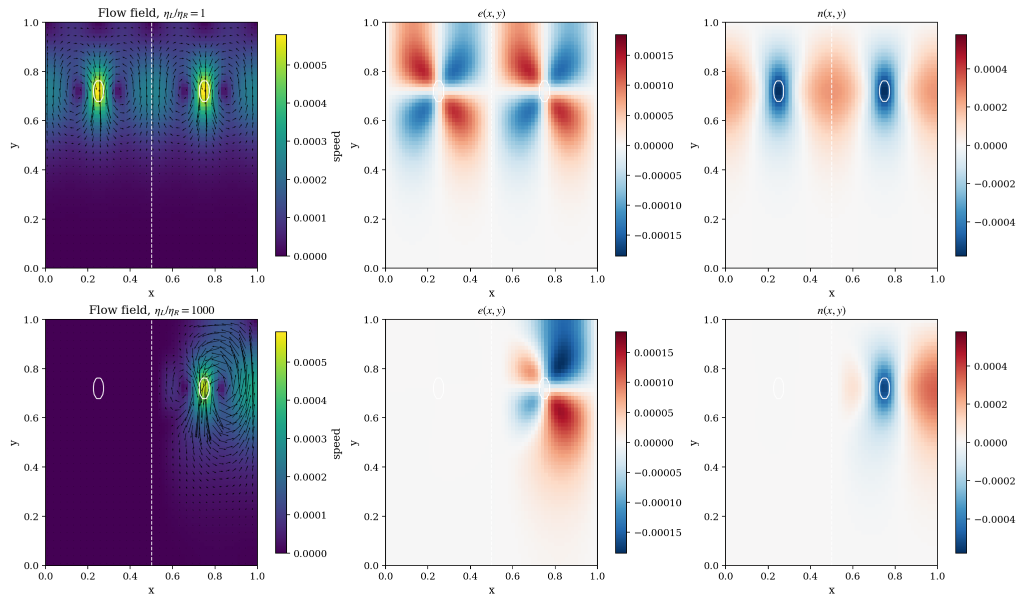

Figure 6. Flow in the two region Cartesian benchmark. The upper row is isoviscous, with $\eta_L/\eta_R = 1$. The lower row has $\eta_L/\eta_R = 1000$. From left to right, the columns show the velocity magnitude and vectors, the horizontal component $e(x, y)$, and the vertical component $n(x, y)$. White contours mark the two negatively buoyant bodies. The dashed line marks the centre of the viscosity transition. Increasing the viscosity on the left suppresses both the descent of the left body and the circulation that it drives.

To quantify this change, let V_L and V_R be the mean sinking speeds measured over the two bodies. The leading Stokes scaling gives

$$\frac{V_L}{V_R} \sim \frac{\eta_R}{\eta_L} = \frac{1}{\eta_L/\eta_R}. \tag{4.9}$$

Figure 7 compares this relation with the computed velocity ratio. The numerical curve follows the inverse viscosity trend over three orders of magnitude in contrast. At $\eta_L/\eta_R = 1000$, the difference from the ideal scaling is about 6–7%.

That remaining difference has a straightforward interpretation. The viscosity transition has finite width. The buoyant bodies have finite size and occupy a bounded domain. The reported velocities are averages over each body, and the density anomaly is smoothed near its edges. These features modify the quantitative velocity response, so the classical $U \propto \eta^{-1}$ Stokes-sinker scaling provides a physical reference rather than an exact prediction for the calculated velocity ratio.

4.3. *Strong lateral viscosity variation in a spherical shell*

The two preceding Cartesian flow tests establish the accuracy of the transformed formulation in controlled settings and recover the expected physical redistribution of flow across a large viscosity contrast. We now use the spherical spectral formulation of Section 3.8 to examine a distinctly three-dimensional consequence of lateral viscosity variation: the coupling of spherical-harmonic modes and the generation of toroidal motion from an initially poloidal buoyancy response. Two-dimensional Cartesian models can

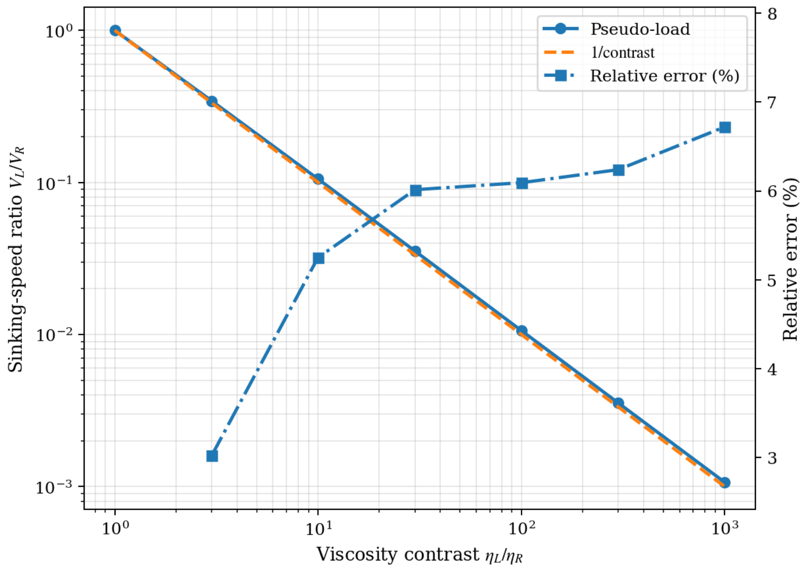

Figure 7. Sinking speed ratio in the two region Cartesian benchmark. The blue curve is the computed ratio V_L/V_R. The orange dashed curve is the inverse viscosity scaling $1/(\eta_L/\eta_R)$. The right axis gives the relative difference between the two. The agreement persists through $\eta_L/\eta_R = 1000$, where the finite transition width, finite body size, and bounded domain account for a remaining difference of about 6–7%.

exhibit viscosity-induced coupling between Fourier modes, but they cannot represent the excitation of toroidal flow or its coupling to poloidal motion. The spherical calculation therefore provides a direct test of the intrinsically three-dimensional part of the coupling structure relevant to planetary interiors. Early three-dimensional calculations demonstrated that lateral viscosity structure can alter mantle flow and its surface expression (Christensen & Harder 1991; Zhang & Christensen 1993; Richards & Hager 1989), while the poloidal–toroidal coupling generated by lateral viscosity was developed explicitly in generalized spherical harmonics by Forte & Peltier (1994). Subsequent studies have explored its consequences for surface velocities, dynamic topography and the geoid (Čadek & Fleitout 2003; Kaban *et al.* 2007; Moucha *et al.* 2007; Rogozhina 2008; Petrunin *et al.* 2013).

We consider a deliberately simple spherical-shell configuration that isolates this mode coupling while allowing the viscosity contrast to be increased strongly. The shell extends from 3480 to 6371 km radius and the reference density is $\rho_0 = 4500\ \mathrm{kg\,m^{-3}}$, and the reference viscosity is $\eta_0 = 10^{21}$ Pa s.

Buoyancy is imposed through a degree-two, order-zero density perturbation localized at $r_b = 5671$ km, corresponding to a depth of 700 km:

$$\delta\rho(r,\theta,\phi) = \rho_0 \frac{A_{20}}{r_b^2}\,\delta(r - r_b)\,Y_{20}(\theta,\phi), \tag{4.10}$$

with

$$A_{20} = 6.43205 \times 10^{15}\ \mathrm{m}^3.$$

The normalization gives $A_{20}/r_b^2 = 200$ m, equal to the radially integrated density anomaly of a fractional perturbation $\delta\rho/\rho_0 = 10^{-3}$ distributed uniformly through a 200 km layer. The finite layer is therefore used only to give a dimensional interpretation of the sheet strength; the numerical forcing itself remains a zero-thickness radial Dirac sheet (Fig. 8a).

The lateral viscosity structure has degree and order $(L_\eta, m_\eta) = (16, 8)$. Its depth dependence is concentrated in a shallow surface layer. The principal transition is centred near 200 km depth, and the amplitude decreases rapidly below this depth over a vertical interval of approximately 40 km (Fig. 8a). The radial variation is smooth and satisfies $\partial_r \Lambda = 0$ at both shell boundaries, so the homogeneous reference boundary conditions derived in Section 3.8 apply directly. We write

$$\Lambda = \ln\left(\frac{\eta}{\eta_0}\right) \tag{4.11}$$

and choose its amplitude so that

$$\frac{\eta_{\max}}{\eta_{\min}} = 10^4. \tag{4.12}$$

The reference viscosity η_0 remains the fixed value introduced above. The lateral viscosity field is constructed so that its logarithmic departure from this reference value has zero horizontal mean at every radius,

$$\langle \Lambda \rangle_H = \left\langle \ln\left(\frac{\eta}{\eta_0}\right) \right\rangle_H = 0.$$

It follows that the fixed reference viscosity is also the horizontal geometric mean of the prescribed viscosity field,

$$\exp\langle \ln \eta \rangle_H = \eta_0.$$

This normalization does not imply that the arithmetic horizontal mean is η_0. Since $\eta = \eta_0 e^{\Lambda}$,

$$\langle \eta \rangle_H = \eta_0 \left\langle e^{\Lambda} \right\rangle_H \geq \eta_0,$$

with strict inequality wherever the lateral viscosity field is nonuniform, by Jensen's inequality (Jensen 1906).

Figure 8 presents the prescribed structure and the resulting surface flow. Panel (a) shows the shallow radial envelope of the lateral viscosity field and the depth of the density sheet; panel (b) shows the surface pattern of Λ. Panels (c) and (d) display, respectively, the renormalized and physical horizontal velocities. Their difference is central to the interpretation: the reference Stokes operator acts on $\mathbf{v}$, whereas the material velocity is recovered from Eq. (2.5). For the present viscosity contrast, the reconstructed physical surface flow reaches a maximum horizontal speed of 10.3256 cm yr^{-1}.

The self-consistent reference-operator problem derived in Section 3.8 is solved here by a relaxed fixed-point iteration, as defined in equation (4.8). At each update, the momentum pseudo-load (3.72) and transformed mass source (3.74) are recomputed from the current renormalized velocity. The fixed buoyancy source is then added and the same constant-reference Green solution operator $\mathcal{G}_0$ is applied again. The spherical calculations use a relaxation factor $\alpha = 0.5$ in (4.8). Thus the analytical reference operator is reused throughout the calculation, while the lateral-viscosity coupling enters entirely through the evolving source pair. The closed-form Green kernels underlying $\mathcal{G}_0$ are given in Appendix B, and the numerical stopping and resolution tests are reported in the Supplementary Material.

A resolution-matched isoviscous calculation provides the physical reference against which to measure the effect of the lateral viscosity field. The buoyancy forcing, shell geometry, boundary conditions, reference viscosity, angular and radial resolution, quadrature and physical reconstruction are identical to those of the 10^4 calculation; only the amplitude

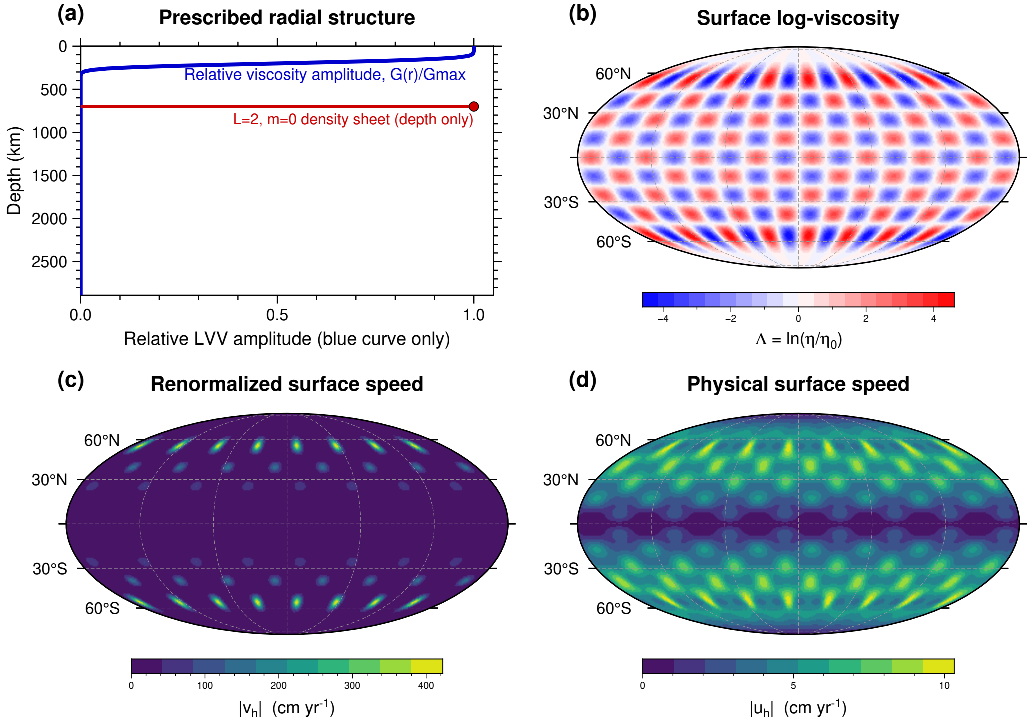

Figure 8. Prescribed structure and surface response of the spherical calculation with $\eta_{\max}/\eta_{\min} = 10^4$. (a) Radial envelope of the imposed $(L_\eta, m_\eta) = (16, 8)$ logarithmic viscosity field. The red line marks the depth of the exact $(s, m) = (2, 0)$ buoyancy sheet at 700 km. It is a depth marker, not a representation of a finite source thickness. (b) Surface $\Lambda = \ln(\eta/\eta_0)$. (c) Magnitude of the renormalized surface horizontal velocity $|\mathbf{v}_h|$, the variable on which the reference Stokes operator acts. (d) Magnitude of the reconstructed physical surface horizontal velocity $|\mathbf{u}_h|$. Coastlines are omitted because the lateral structure is an ideal harmonic pattern rather than a geographic model.

of the lateral viscosity variation is set to zero. Hence

$$\Lambda = 0, \qquad \frac{\eta}{\eta_0} = 1, \qquad \mathbf{v} = \mathbf{u} \tag{4.13}$$

to machine precision. Figure 9 shows the resulting response. The degree-two buoyancy sheet produces the analytic isoviscous poloidal flow predicted by the reference Green functions (Forte & Peltier 1987): the maximum surface horizontal speed is 6.0347 cm yr^{-1}, the RMS horizontal divergence is 0.169448 rad/10 Myr, and the divergence spectrum is confined to $\ell = 2$ to numerical precision. Only 3.9×10^{-24} of its divergence variance lies outside degree two. The RMS radial vorticity is 1.68×10^{-13} rad/10 Myr, effectively zero on the scale of the calculation. The isoviscous control solution therefore establishes a sharply defined baseline: specifically, that all resolved toroidal motion and all substantial power outside the directly forced degree in the strong-LVV calculation are generated by the lateral viscosity field.

The final 10^4-contrast calculation uses $L_{\max} = 180$, $N_r = 161$, and product quadrature order 161. The physical velocity is reconstructed through degree 276 because multiplication by $e^{-\Lambda}$ broadens its harmonic content beyond the spectral range solved directly for the reference problem. The resolution tests show that the interpreted flow is well separated from the truncation boundary. At contrast 10^3, increasing N_r from 129 to 161 changes representative resolved quantities by approximately 10^{-8} to 5×10^{-7} in relative terms.

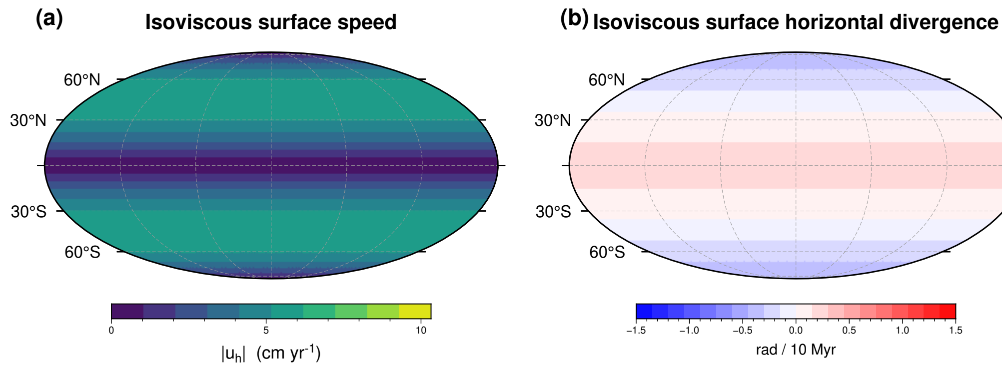

Figure 9. Resolution-matched isoviscous control for the spherical calculation. (a) Magnitude of the physical surface horizontal velocity. (b) Physical surface horizontal divergence in the Forte–Peltier normalization. Every parameter apart from the amplitude of the lateral viscosity field is the same as in Fig. 8. Panel (a) uses the same 0–10.3256 cm yr^{-1} colour scale as Fig. 8(d), and panel (b) uses the same $[-1.5, +1.5]$ rad/10 Myr scale as Fig. 10(a).

At contrast 10^4, increasing $L_{\max}$ from 144 to 180 reduces the retained spectral tail by about 3.6×10^3 and the discarded-source measure by about 3.1×10^3, while the whole-shell L^2 norm of the renormalized velocity and its toroidal fraction change by only a few parts in 10^9. The final calculation converges after 49 fixed-point updates, with a final state update of 7.95×10^{-9} and an operator-consistent transformed-mass residual of 2.45×10^{-8}. Independent tests of the reference Green solution operator and the generalized spherical-harmonic transforms are at the 10^{-14} level. The full radial, angular, operator and reconstruction audits are given in Sections S2–S4 of the Supplementary Material, while the degree-one rotational null space is treated in Appendix A and evaluated numerically in Section S5.

We now turn to the physical spectral response. Section 3.8 shows that, at an impermeable surface, the horizontal divergence D and radial vorticity R isolate the poloidal and toroidal parts of the physical surface velocity [Eq. (3.96)]. The same section also gives the general harmonic selection rules for viscosity-induced coupling. Applied to the present degree-two poloidal forcing and degree-16 viscosity field, Eqs. (3.98) and (3.99) predict the first coupled generation

$$\text{Poloidal } (P): \ \ell = 14, 16, 18, \qquad \text{Toroidal } (T): \ \ell = 15, 17. \tag{4.14}$$

Because $L_\eta = 16$ is even, repeated coupling preserves the parity sequence

$$P_{\text{even}} \longrightarrow T_{\text{odd}} \longrightarrow P_{\text{even}} \longrightarrow \cdots . \tag{4.15}$$

The imposed azimuthal structure is equally restrictive: the $m = 0$ buoyancy and $m = \pm 8$ viscosity harmonics generate orders that are multiples of eight. The alternating empty degrees and the eightfold map symmetry are therefore direct spectral signatures of this controlled coupling geometry.

Figure 10 shows the response after this coupling has acted to convergence. The surface horizontal divergence has

$$D_{\text{rms}} = 0.336198 \text{ rad}/10\,\text{Myr}, \tag{4.16}$$

while the radial vorticity has

$$R_{\text{rms}} = 0.229972 \text{ rad}/10\,\text{Myr}. \tag{4.17}$$

Thus

$$\frac{R_{\rm rms}}{D_{\rm rms}} = 0.684. \tag{4.18}$$

The isoviscous reference has essentially zero radial vorticity, so the finite rotational surface field in Fig. 10(b) is a direct consequence of the lateral viscosity coupling. The free-slip shell admits a separate degree-one rigid-rotation null mode; the zero-angular-momentum condition of Appendix A fixes only that arbitrary frame freedom and retains any torque-compatible differential rotation. Its numerical enforcement leaves degree-one radial vorticity at a negligible level, as documented in Section S5 of the Supplementary Material.

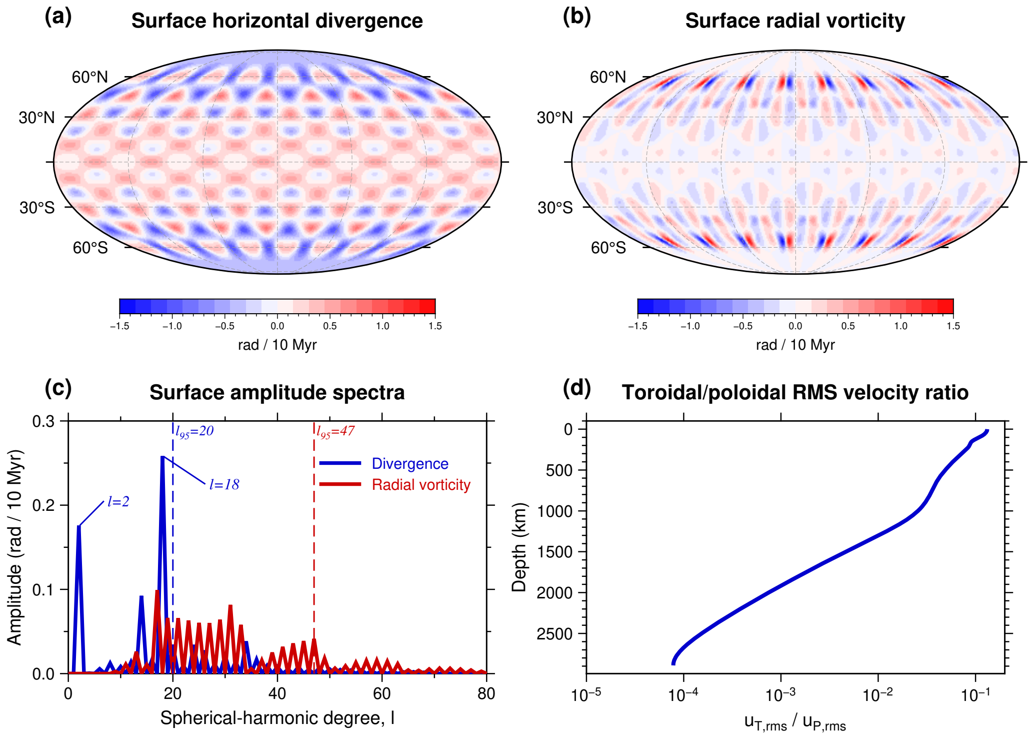

Figure 10. Physical diagnostics for the spherical calculation with a viscosity contrast of 10^4. (a) Surface horizontal divergence. (b) Surface radial vorticity. The two maps use the same Forte–Peltier normalization and the same symmetric range of $[-1.5, +1.5]$ rad/10 Myr. (c) Degree amplitudes of surface divergence in blue and radial vorticity in red. The dashed markers give ℓ_{95}, defined as the smallest degree containing at least 95% of the cumulative squared degree amplitude. The values are $\ell_{95} = 20$ for divergence and $\ell_{95} = 47$ for radial vorticity. The labelled degree-two and degree-18 divergence peaks distinguish the directly forced response from the strongest member of the first poloidal band opened by viscosity coupling. (d) RMS toroidal-to-poloidal velocity amplitude ratio as a function of depth, $u_{T,\rm rms}/u_{P,\rm rms} = \sqrt{E_T/E_P}$. The map grids are interpolated at one-degree spacing for display only; all quoted spectra and RMS quantities are evaluated directly from the spectral solution.

The matched isoviscous control solution makes the amplitude redistribution in Fig. 10(c) especially clear. Introducing the lateral viscosity variation raises the divergence RMS from 0.169448 to 0.336198 rad/10 Myr, an increase by a factor of 1.984. The directly forced $\ell = 2$ component changes much less, from 0.169448 to approximately 0.175751 rad/10 Myr, or about 3.7%. The near doubling of the total divergence therefore comes primarily from power transferred into additional harmonics rather than from amplification of the original degree-two pattern.

Degree 18 provides the clearest example. It belongs to the first poloidal band predicted by Eq. (4.14), and its divergence amplitude is approximately 0.2583 rad/10 Myr. This exceeds the degree-two amplitude of the isoviscous control by a factor of about 1.52 and the degree-two amplitude of the strong-LVV calculation by a factor of about 1.47. Because horizontal divergence contains angular derivatives, shorter wavelengths are weighted more strongly than in the velocity itself. The degree-18 peak therefore records a substantial transfer of the surface-gradient field toward shorter spatial scales, exactly where the spherical coupling rules first permit it.

The toroidal response is broader still. Ninety-five per cent of the cumulative squared degree amplitude is reached by $\ell = 20$ for divergence but only by $\ell = 47$ for radial vorticity. The physical surface velocity consequently has a substantial radial vorticity. The toroidal-to-poloidal squared-velocity-norm ratio is 1.7423×10^{-2}, corresponding to the RMS amplitude ratio

$$\frac{u_{T,\mathrm{rms}}}{u_{P,\mathrm{rms}}} = 0.132. \tag{4.19}$$

The ratio decreases rapidly below the shallow viscosity structure, reaching approximately 5.72×10^{-3} at mid-shell and 7.8×10^{-5} near the lower boundary (Fig. 10a). The rotational flow is therefore most strongly expressed where the imposed lateral viscosity gradients are largest and weakens sharply beneath that layer.

The renormalized and physical velocity fields also partition differently between poloidal and toroidal components. This distinction is made clear in Section 3.8, because the physical reconstruction is a local multiplication by $e^{-\Lambda}$, whereas the poloidal–toroidal decomposition is a global differential operation, and the two do not commute [Eq. (3.97)]. In this calculation the toroidal part accounts for about 0.498 of the squared velocity norm of $\mathbf{v}$, but only 4.14×10^{-3} of the corresponding whole-shell norm of $\mathbf{u}$. The contrast between these values is itself a consequence of the strong harmonic mixing introduced by reconstruction and reinforces the need to interpret the material flow through $\mathbf{u}$, not through the renormalized field alone.

Figure 10 clearly shows that strong lateral viscosity gradients induce a strong primary degree-18 poloidal response, substantial shorter-wavelength spectral power, and a broad-spectrum toroidal field expressed directly as surface radial vorticity. The intentionally simple harmonic geometry we employed makes each of these pathways in spectral space identifiable against the selection rules of Section 3.8. In a viscosity field with broad spectral content, many such pathways will operate simultaneously, but the coupling mechanisms isolated here remain the same. Strong lateral viscosity variation does not merely rescale the buoyancy-driven circulation. It reorganizes that circulation across spherical-harmonic degree and couples poloidal and toroidal motion in fully three-dimensional spherical geometry.

5. Conclusions

The central result of this study is an exact reformulation of the variable-viscosity Stokes equations that exposes $\nabla \ln \eta$ as the natural field governing the coupling introduced by spatial viscosity heterogeneity. For a prescribed, positive Newtonian viscosity field, the exact transformation

$$\Lambda = \ln\left(\frac{\eta}{\eta_0}\right), \qquad \mathbf{v} = \left(\frac{\eta}{\eta_0}\right)\mathbf{u},$$

identifies

$$\boldsymbol{\xi} = \nabla \Lambda = \nabla \ln\left(\frac{\eta}{\eta_0}\right) = \frac{\nabla \eta}{\eta}$$

as the natural local measure of viscosity heterogeneity. This distinction is both physical and numerical. The absolute viscosity scale controls the conversion between the renormalized velocity $\mathbf{v}$ and the physical velocity $\mathbf{u}$, while the coupling produced by spatial viscosity variation is governed by the magnitude, direction and spatial structure of $\boldsymbol{\xi}$. A uniform rescaling of the complete viscosity field changes the physical velocity amplitude but leaves $\boldsymbol{\xi}$ unchanged. Large multiplicative contrasts in viscosity therefore become additive variations in Λ, and their dynamical influence is organized through the spatial gradients of this logarithmic field.

This structure leads directly to the numerical formulation developed here. A chosen reference Stokes operator can be retained, while the remaining viscosity heterogeneity enters through pseudo-load terms constructed from $\mathbf{v}$ and $\boldsymbol{\xi}$, together with the corresponding source in the transformed mass constraint. The Cartesian calculations verify the transformed equations in two complementary settings. The manufactured solution tests the formulation against an exact velocity and pressure field, and the two region calculation recovers the expected redistribution of flow across a strong viscosity contrast. These tests establish the consistency of the transformation and its implementation. They also show why the usefulness of the method is not determined by viscosity contrast alone: the spatial structure carried by $\nabla\Lambda$ is central to the conditioning of the coupled problem.

The spherical shell calculation in Section 4.3 provides the most direct expression of this result. In the isoviscous control, a degree two buoyancy source produces the expected degree two poloidal flow, with vanishingly small toroidal motion. Introducing a degree 16, order 8 viscosity field with a contrast of 10^4 changes the problem qualitatively. The viscosity gradient couples the directly forced mode into the poloidal and toroidal spectral locations permitted by generalized spherical harmonic theory (Forte & Peltier 1994). The surface divergence develops a strong degree 18 response and substantial power outside the directly forced degree. Radial vorticity, absent from the isoviscous control, appears over a much broader range of degrees. This toroidal contribution is strongest near the surface and decreases rapidly with depth. Lateral viscosity variation therefore does more than rescale an existing flow. Through the geometry and spectral content of $\nabla\Lambda$, it redistributes the flow among spatial scales and converts part of the buoyancy driven poloidal circulation into toroidal motion.

This controlled experiment also clarifies what should be meant by a "strong" viscosity variation. A large value of $\eta_{\max}/\eta_{\min}$ is not, by itself, a complete measure of the strength of the coupling. Two viscosity fields with the same contrast can produce very different Stokes problems if one is smooth and the other contains sharp or short wavelength structure. The latter has larger and broader gradients of logarithmic viscosity and can generate a stronger and wider spectrum pseudo-load. The important quantities are therefore the amplitude and geometry of $\nabla\Lambda$, its radial and angular bandwidth, and its relation to the chosen reference viscosity. This interpretation connects the mathematical transformation directly to the physical redistribution seen in Section 4.3.

The numerical certification of the spherical calculation, detailed in the Supplement, was designed to test this redistribution independently at each stage. Radial and angular refinement establish that the imposed viscosity structure and the generated spectral bandwidth are resolved. Exact reference operator and harmonic transform tests verify the underlying inverse. Reconstruction of the physical velocity tests the transformation back from $\mathbf{v}$ to $\mathbf{u}$, and the angular momentum constraint fixes the physical rotational frame.

Together these tests establish that poloidal–toroidal coupling at a viscosity contrast of 10^4 is fully resolved by the numerics.

The spherical calculation isolates the three-dimensional mode-coupling mechanism in a form that can be compared directly with the underlying harmonic theory. The prescribed Newtonian viscosity provides a controlled setting in which the roles of viscosity geometry, spectral content and $\nabla \ln \eta$ can be identified unambiguously. More general mantle rheologies may introduce additional dependence on stress, strain rate, grain size, composition and thermal evolution, requiring these variables to be coupled self-consistently to the viscosity field. Such extensions modify the constitutive closure, but not the exact logarithmic-viscosity transformation of the Stokes equations developed here.

A first step toward those applications has already been made by Kamali Lima (2026). There the same logarithmic viscosity structure is used in a spherical spectral Stokes solver with generalized spherical harmonics, pseudospectral evaluation of the viscosity coupling and a preconditioned Picard–Krylov solution. Three-dimensional temperature-dependent viscosity models spanning approximately one to four orders of magnitude in upper mantle contrast were solved without damping of the outer iteration. In the strongest case, the calculation converged in 49 outer iterations on 128 MPI ranks. The resulting lateral viscosity variations produce large changes in the predicted geoid, free air gravity and dynamic topography, and generate substantial toroidal motion at intermediate and short wavelengths. The same doctoral study extends the calculation to lithospheric weak zones along plate boundaries. These models focus horizontal divergence and radial vorticity around the weak zone network, showing directly that the geometry of $\nabla \Lambda$ controls where deformation and toroidal shear are localized. These calculations offer a production-stream implementation of the logarithmic viscosity framework examined here, and form the basis of forthcoming work on global mantle flow with strong three dimensional viscosity structure.

The longer term direction is to make the three dimensional rheology itself the primary model rather than treating lateral structure as an addition to an independently inferred one dimensional viscosity profile. A physically constrained field $\Lambda(r, \theta, \phi)$, informed by temperature, composition and lithospheric weakening, can define both the full viscosity and the radial reference used by the numerical solver. This would allow the reference profile to be derived consistently from the same three dimensional rheology and would reduce ambiguity in separating radial and lateral effects. The logarithmic formulation is especially well suited to this development because it places the physically relevant heterogeneity in $\nabla \Lambda$ while preserving a practical reference operator. The controlled results presented here establish the mathematical and numerical foundation for that progression from isolated coupling tests to global models in which strong, spatially localized viscosity variations participate directly in the mantle flow and its observable surface expression.

Declaration of Interests.
The authors report no conflict of interest.

Acknowledgments
The authors wish to thank Petar Glišović and Shangxin Liu for lengthy discussions and helpful suggestions. The authors also acknowledge the support provided by the French "Programme d'investissements d'avenir" under the auspices of the GYPTIS project – ANR 19 MPGA 0007 and the support provided by the Institut de Physique du Globe de Paris. AMF acknowledges support from the University of Florida and the support of this work provided by NSF grant EAR 1903108.

Appendix A. Degree-one toroidal motion: the zero-angular-momentum frame

Here, we focus on the degree-one toroidal response because care must be taken in treating both a true differential rotation and an arbitrary rigid rotation. These are physically distinct, although they both have the same degree-one geometry. The distinction between rigid degree-one rotation and depth-dependent differential rotation in a laterally heterogeneous mantle was discussed explicitly by Forte & Peltier (1994), together with the angular momentum carried by the degree-one toroidal flow. Zhang & Christensen (1993) likewise identified the singular degree-one toroidal freedom in their transformed spherical formulation, distinguishing the dynamically constrained differential rotation from the arbitrary rigid-body component and noting the difficulty of assigning a physical meaning to the rotational gauge in their viscosity-scaled variables. Related analyses of differential lithosphere–mantle rotation include Ricard *et al.* (1991), while angular-momentum-based removal of arbitrary whole-mantle rotation has also been used in three-dimensional spherical convection calculations (Zhong *et al.* 2008). The transformed problem considered below adds a further distinction: the rigid null space belongs to the reference velocity $\mathbf{v}$, whereas the physical frame condition must be imposed on the reconstructed velocity $\mathbf{u}$.

A degree-one toroidal field can be written without reference to a particular spherical harmonic normalization as

$$\mathbf{w}_1^T(r,\theta,\phi) = \boldsymbol{\omega}(r) \times \boldsymbol{r}. \tag{A 1}$$

For the reference problem below, $\mathbf{w} = \mathbf{v}$. The vector $\boldsymbol{\omega}(r)$ is the angular velocity of the spherical surface at radius r. If it is independent of radius, the entire shell undergoes rigid rotation. The strain rate then vanishes and the motion produces no Newtonian viscous stress. If $\boldsymbol{\omega}$ varies with radius, different spherical surfaces rotate at different rates or about different axes. That part of the motion is a differential rotation with shear and is therefore a physically determined component of the flow, not an arbitrary rigid-body rotation. The spherical spectral representation and its relation to the classical poloidal–toroidal decomposition are developed in Section 3.8, following the generalized spherical-harmonic representation employed in Forte & Peltier (1994).

Using the vector spherical harmonic representation (3.65) introduced in Section 3.8, let $W_{\ell m}^{(v)}(r)$ denote the toroidal coefficient of the renormalized velocity. It multiplies $\hat{\boldsymbol{r}} \times \nabla_1 Y_{\ell m}$ and therefore controls the radial vorticity associated with degree ℓ and order m. For the constant-viscosity reference problem, its radial equation has the form

$$\eta_0 \mathcal{D}_\ell W_{\ell m}^{(v)} = Q_{\ell m}^T, \tag{A 2}$$

where $\mathcal{D}_\ell$ is the radial operator defined in Eq. (3.87) and $Q_{\ell m}^T$ is the toroidal projection of the effective momentum source. The factor η_0 is retained explicitly so that the normalization is identical to Eq. (3.92). Homogeneous free slip at the inner and outer radii, b and a, requires

$$\left(\frac{\mathrm{d}W_{\ell m}^{(v)}}{\mathrm{d}r} - \frac{W_{\ell m}^{(v)}}{r} \right)_{r=b,a} = 0. \tag{A 3}$$

At $\ell = 1$, the homogeneous solution $W = r$ satisfies both the differential equation and the two free slip conditions. The reference operator is therefore singular in precisely the manner expected for a rigid rotation. A forced solution may be written as

$$W_{1m}^{(v)}(r) = W_{1m,\mathrm{diff}}^{(v)}(r) + C_m r. \tag{A 4}$$

The effective load determines the differential part $W_{1m,\mathrm{diff}}^{(v)}$. The coefficient C_m remains undetermined because adding a rigid rotation does not change the reference viscous stress. Equation (A 4) makes clear that removing the whole degree-one toroidal sector would therefore remove a physical differential response together with the arbitrary rigid component. Only the latter is a degree of freedom.

The singular radial equation also places a compatibility condition on its forcing. Define

$$\Omega_m^{(v)}(r) = \frac{W_{1m}^{(v)}(r)}{r}. \tag{A 5}$$

Equation (A 2) then becomes, at degree one,

$$\frac{\eta_0}{r^3} \frac{\mathrm{d}}{\mathrm{d}r} \left(r^4 \frac{\mathrm{d}\Omega_m^{(v)}}{\mathrm{d}r} \right) = Q_{1m}^T(r). \tag{A 6}$$

The free slip conditions reduce to $\Omega_m^{(v)\prime}(b) = \Omega_m^{(v)\prime}(a) = 0$. Integration across the shell therefore gives

$$\int_b^a r^3 Q_{1m}^T(r)\,\mathrm{d}r = 0. \tag{A 7}$$

This is the solvability condition for the singular reference problem. Its physical meaning is that in the absence of an applied boundary torque, the effective volume load must exert no net torque on the shell.

Torque compatibility tells us that the forced differential solution can exist, but it does not determine the rotational frame in which that solution is reported. These are two separate parts of the degree-one problem. Equation (A 7) constrains the forcing. Once that condition is satisfied, the reference Stokes equations still admit an arbitrary rigid rotation, and that remaining freedom must be fixed in the space of the reconstructed physical velocity.

To make this distinction explicit, we write the three real rigid rotations of the reference problem as

$$\boldsymbol{\phi}_j(\boldsymbol{r}) = \boldsymbol{e}_j \times \boldsymbol{r}, \qquad j = 1, 2, 3, \tag{A 8}$$

where $\boldsymbol{e}_j$ are Cartesian unit vectors. If $\mathbf{v}_{\mathrm{diff}}$ denotes a torque-compatible differential-rotation solution, then every member of the family

$$\mathbf{v} = \mathbf{v}_{\mathrm{diff}} + \sum_{j=1}^{3} C_j \boldsymbol{\phi}_j \tag{A 9}$$

satisfies the same reference momentum equation. The coefficients C_j therefore describe only the undetermined rigid-rotation coordinates of the reference problem and they do not change its forced differential response.

The physical velocity is obtained after the logarithmic-viscosity transformation is reversed,

$$\mathbf{u} = e^{-\Lambda}\mathbf{v}_{\mathrm{diff}} + e^{-\Lambda} \sum_{j=1}^{3} C_j \boldsymbol{\phi}_j. \tag{A 10}$$

This expression is key to the subsequent determination of the frame. When Λ varies laterally, multiplication by $e^{-\Lambda}$ couples spherical harmonics. A rigid null mode in the reference velocity $\mathbf{v}$ therefore does not, in general, remain a pure rigid rotation in the physical velocity $\mathbf{u}$. The degree of freedom belongs to the reference problem, in transformed velocity space, whereas the frame condition must be imposed on the physical flow.

We choose that frame by requiring the residual convective velocity to carry no net angular momentum,

$$\mathcal{J}[\mathbf{u}] = \int_V \rho_0(r)\, \boldsymbol{r} \times \mathbf{u} \, \mathrm{d}V = \mathbf{0}. \tag{A 11}$$

Here $\mathcal{J}$ is the angular momentum of the residual convective motion in the adopted rotating frame. It should be understood that equation (A 11) does not refer to the total rotational angular momentum of the planet.

The remaining algebra can interpreted as a response problem. We write

$$\boldsymbol{M}_0 = \mathcal{J}\left[e^{-\Lambda}\mathbf{v}_{\mathrm{diff}}\right] \tag{A 12}$$

to represent the physical angular momentum of the provisional differential solution. The jth column of the response matrix records the physical angular momentum produced by adding a unit amplitude of the jth exact reference null mode:

$$A_{ij} = \boldsymbol{e}_i \cdot \mathcal{J}\left[e^{-\Lambda}\boldsymbol{\phi}_j\right]. \tag{A 13}$$

Thus A is simply the linear map from rigid-rotation amplitudes in the reference velocity to angular momentum in the reconstructed physical velocity. For a coefficient vector $\boldsymbol{C} = (C_1, C_2, C_3)^{\mathsf{T}}$, the physical moment is

$$\mathcal{J}[\mathbf{u}] = \boldsymbol{M}_0 + \mathsf{A}\boldsymbol{C}. \tag{A 14}$$

Imposing Eq. (A 11) therefore gives

$$\boldsymbol{C} = -\mathsf{A}^{-1}\boldsymbol{M}_0. \tag{A 15}$$

This correction is unique. To understand this, let us consider any nonzero trial rotation vector $\boldsymbol{\Omega}$. The corresponding reference-null velocity is $\delta\mathbf{v} = \boldsymbol{\Omega} \times \boldsymbol{r}$, and its physical counterpart is $e^{-\Lambda}\delta\mathbf{v}$. Projecting the resulting physical angular momentum onto the same rotation vector gives

$$\boldsymbol{\Omega}^{\mathsf{T}}\mathsf{A}\boldsymbol{\Omega} = \int_V \rho_0(r) e^{-\Lambda} \left|\boldsymbol{\Omega} \times \boldsymbol{r}\right|^2 \mathrm{d}V > 0, \tag{A 16}$$

for every $\boldsymbol{\Omega} \neq \mathbf{0}$. The response matrix is therefore positive definite on the active rotational subspace and cannot map a nonzero admissible rigid rotation to zero physical angular-momentum response.

The construction satisfies the two requirements simultaneously. Because the correction added to $\mathbf{v}$ lies entirely in the exact rigid null space, the reference momentum equation and its differential degree-one toroidal response are unchanged. Because the amplitudes are chosen through Eq. (A 15), the reconstructed physical velocity satisfies the zero-angular-momentum frame condition.

In the general three-dimensional problem, A acts on three real rotation coordinates. Symmetry can reduce that active space. In the spherical benchmark of Section 4.3, the buoyancy forcing is axisymmetric ($m = 0$) and the viscosity field has $m = \pm 8$. Repeated coupling therefore remains within azimuthal orders that are multiples of eight. Degree one, however, admits only $m = -1, 0, 1$. The only order common to these two sets is $m = 0$, corresponding to rotation about the symmetry axis. Accordingly, the three-dimensional frame problem reduces to a single axial null coordinate in this particular benchmark. The reduction follows simply as a consequence of the imposed symmetry.

The numerical tests of torque compatibility, the response matrix, the physical angular momentum residual, and the surviving degree-one rotation are reported in Section S5 of the Supplementary Material.

The key result that emerges from the treatment presented here is that the singular degree-one reference equation must retain its compatible differential response, and the remaining rigid freedom must be fixed by applying a condition to the reconstructed physical velocity.

Appendix B. Closed-form Green kernels for the spherical reference Stokes operator

Section 3.8 reduces the constant-reference spherical problem to three radial responses: force-driven poloidal flow, force-driven toroidal flow, and the additional spheroidal response to the transformed mass source. We collect here the corresponding closed-form kernels in the notation of that section. The poloidal kernel is the biharmonic Green function of Forte & Peltier (1987), written in a ratio-scaled form; the toroidal and transformed-mass kernels complete the Green solution operator $\mathcal{G}_0$ defined in Eq. (3.85).

Let

$$q = \frac{b}{a}, \qquad x = \frac{r}{a}, \qquad y = \frac{r'}{a}, \qquad L = \ell(\ell+1), \tag{B 1}$$

with $q \le x, y \le 1$, and define the dimensionless radial operator

$$\mathcal{L}_\ell f = \frac{\mathrm{d}^2 f}{\mathrm{d}x^2} + \frac{2}{x}\frac{\mathrm{d}f}{\mathrm{d}x} - \frac{L}{x^2} f. \tag{B 2}$$

The dimensional primitive kernels used below satisfy

$$G_\ell^P(r,r') = a^3 g_\ell(x,y), \qquad G_\ell^T(r,r') = a\, t_\ell(x,y), \qquad N_\ell(r,r') = a\, n_\ell(x,y), \qquad K_\ell^M(r,r') = a\, k_\ell^M(x,y). \tag{B 3}$$

B.1. *Force-driven poloidal response*

The closed-form isoviscous Green functions for the force-driven poloidal velocity and its associated dynamic pressure used here follow Forte & Peltier (1987). Here we write these results in the vector spherical harmonic notation adopted in Section 3.8 and recast the radial kernels in a ratio-scaled form that is algebraically equivalent to the original expressions and convenient for stable high-degree evaluation.

For $\ell \ge 1$, define g_ℓ by

$$\mathcal{L}_\ell^2 g_\ell(x,y) = \delta(x-y), \qquad g_\ell = \partial_x^2 g_\ell = 0 \quad \text{at} \quad x = q, 1. \tag{B 4}$$

The exact ratio-scaled form is, for $x \le y$,

$$g_\ell^<(x,y) = \frac{y^3}{2(2\ell+1)}\left[\frac{(x/y)^\ell}{2\ell-1}\,\frac{[1-(q/x)^{2\ell-1}][1-y^{2\ell-1}]}{1-q^{2\ell-1}} - \frac{(x/y)^{\ell+2}}{2\ell+3}\,\frac{[1-(q/x)^{2\ell+3}][1-y^{2\ell+3}]}{1-q^{2\ell+3}}\right], \tag{B 5}$$

and, for $x \ge y$,

$$g_\ell^>(x,y) = \frac{y^3}{2(2\ell+1)}\left[\frac{(y/x)^{\ell-1}}{2\ell-1}\,\frac{[1-(q/y)^{2\ell-1}][1-x^{2\ell-1}]}{1-q^{2\ell-1}} - \frac{(y/x)^{\ell+1}}{2\ell+3}\,\frac{[1-(q/y)^{2\ell+3}][1-x^{2\ell+3}]}{1-q^{2\ell+3}}\right]. \tag{B 6}$$

The kernel and its first two field derivatives are continuous at $x = y$, while $[\partial_x^3 g_\ell]_{y^-}^{y^+} = 1$. These conditions, together with Eq. (B 4), uniquely specify the biharmonic inverse.

To write the complete force-to-velocity block compactly, define, branchwise,

$$R_0 = -\frac{g_\ell}{y}, \qquad S_0 = \frac{g_\ell}{y} - \partial_y g_\ell, \qquad R_j = \partial_x^j R_0, \qquad S_j = \partial_x^j S_0 \quad (j = 1,2,3). \tag{B 7}$$

The dimensionless poloidal velocity kernels are

$$\mathcal{G}_\ell^{UR} = \frac{L}{x} R_0, \qquad \mathcal{G}_\ell^{VR} = R_1 + \frac{R_0}{x}, \tag{B 8}$$

$$\mathcal{G}_\ell^{US} = \frac{L}{x} S_0, \qquad \mathcal{G}_\ell^{VS} = S_1 + \frac{S_0}{x}, \tag{B 9}$$

and the corresponding pressure kernels are

$$\mathcal{P}_\ell^{R} = xR_3 + 3R_2 - \frac{L}{x} R_1 + \frac{L}{x^2} R_0, \tag{B 10}$$

$$\mathcal{P}_\ell^{S} = xS_3 + 3S_2 - \frac{L}{x} S_1 + \frac{L}{x^2} S_0. \tag{B 11}$$

All derivatives in Eqs. (B 7)– (B 11) are analytic derivatives of Eqs. (B 5) and (B 6); no numerical source differentiation is required.

B.2. *Force-driven toroidal response*

For $\ell \geq 2$, put

$$n = 2\ell + 1, \qquad \kappa_\ell = \frac{\ell - 1}{\ell + 2}. \tag{B 12}$$

The exact toroidal kernel is

$$t_\ell^{<}(x, y) = -\frac{y}{n(1 - q^n)} \left(\frac{x}{y}\right)^{\ell} \left[1 + \kappa_\ell \left(\frac{q}{x}\right)^{n}\right] \left(1 + \frac{y^n}{\kappa_\ell}\right), \qquad x \leq y, \tag{B 13}$$

and

$$t_\ell^{>}(x, y) = -\frac{y}{n(1 - q^n)} \left(\frac{y}{x}\right)^{\ell+1} \left[1 + \kappa_\ell \left(\frac{q}{y}\right)^{n}\right] \left(1 + \frac{x^n}{\kappa_\ell}\right), \qquad x \geq y. \tag{B 14}$$

It satisfies $\mathcal{L}_\ell t_\ell = \delta(x - y)$, is continuous at the source radius, has $[\partial_x t_\ell]_{y^-}^{y^+} = 1$, and obeys the free-slip condition $\partial_x t_\ell - t_\ell / x = 0$ at both boundaries. The singular $\ell = 1$ response is treated in Appendix A.

Combining the poloidal and toroidal kernels, the complete force-driven response is

$$\begin{pmatrix} U^F_{\ell m} \\ V^F_{\ell m} \\ W^F_{\ell m} \end{pmatrix}(r) = \frac{a}{\eta_0} \int_b^a \begin{pmatrix} \mathcal{G}_\ell^{UR} & \mathcal{G}_\ell^{US} & 0 \\ \mathcal{G}_\ell^{VR} & \mathcal{G}_\ell^{VS} & 0 \\ 0 & 0 & t_\ell \end{pmatrix}_{(x,y)} \begin{pmatrix} Q^R_{\ell m} \\ Q^S_{\ell m} \\ Q^T_{\ell m} \end{pmatrix}(r')\, \mathrm{d}r', \tag{B 15}$$

with pressure

$$p^F_{\ell m}(r) = \int_b^a \begin{pmatrix} \mathcal{P}_\ell^R & \mathcal{P}_\ell^S & 0 \end{pmatrix}_{(x,y)} \begin{pmatrix} Q^R_{\ell m} \\ Q^S_{\ell m} \\ Q^T_{\ell m} \end{pmatrix}(r')\, \mathrm{d}r'. \tag{B 16}$$

B.3. *Transformed-mass response*

The scalar source in Eq. (3.76) requires a third, spheroidal Green response. For $\ell \geq 1$, define

$$\alpha_\ell = \frac{\ell}{\ell + 1}, \qquad p = 2\ell + 1. \tag{B 17}$$

The Neumann Poisson kernel is

$$n_\ell(x, y) = -\frac{y}{(2\ell + 1)(1 - q^p)} \begin{cases} (x/y)^\ell [1 + \alpha_\ell (q/x)^p][1 + y^p/\alpha_\ell], & x \leq y, \\ (y/x)^{\ell+1} [1 + \alpha_\ell (q/y)^p][1 + x^p/\alpha_\ell], & x \geq y, \end{cases} \tag{B 18}$$

so that $\mathcal{L}_\ell n_\ell = \delta(x - y)$, $\partial_x n_\ell = 0$ at $x = q, 1$, and $[\partial_x n_\ell]_{y^-}^{y^+} = 1$.

The gradient field generated by n_ℓ supplies the required divergence but not, by itself, zero tangential traction. The divergence-free boundary correction is obtained from

$$F_b(x) = q^{\ell-1}(x^\ell - x^{1-\ell}), \qquad G_b(x) = q^{\ell+1}(x^{-\ell-1} - x^{\ell+2}), \tag{B 19}$$

$$F_a(x) = x^\ell - q^{2\ell-1} x^{1-\ell}, \qquad G_a(x) = q^{2\ell+3} x^{-\ell-1} - x^{\ell+2}, \tag{B 20}$$

with

$$D_b = \frac{2(2\ell+1)}{q^2}(1-q^{2\ell-1})(1-q^{2\ell+3}), \qquad D_a = 2(2\ell+1)(1-q^{2\ell-1})(1-q^{2\ell+3}), \tag{B 21}$$

and

$$h_\ell^b(x) = \frac{G_b(q)F_b(x) - F_b(q)G_b(x)}{D_b}, \qquad h_\ell^a(x) = \frac{G_a(1)F_a(x) - F_a(1)G_a(x)}{D_a}. \tag{B 22}$$

The required biharmonic correction is then

$$k_\ell^M(x,y) = \frac{2n_\ell(q,y)}{q^2} h_\ell^b(x) + 2n_\ell(1,y)h_\ell^a(x). \tag{B 23}$$

The exact mass-to-velocity kernels are

$$G_\ell^{M,U}(x,y) = \partial_x n_\ell(x,y) + \frac{L}{x} k_\ell^M(x,y), \tag{B 24}$$

$$G_\ell^{M,V}(x,y) = \frac{n_\ell(x,y)}{x} + \partial_x k_\ell^M(x,y) + \frac{k_\ell^M(x,y)}{x}. \tag{B 25}$$

Thus

$$U_{\ell m}^M(r) = \int_b^a G_\ell^{M,U}(x,y) s_{\ell m}(r')\,\mathrm{d}r', \qquad V_{\ell m}^M(r) = \int_b^a G_\ell^{M,V}(x,y) s_{\ell m}(r')\,\mathrm{d}r'. \tag{B 26}$$

The associated pressure contains a local term and the pressure of the biharmonic boundary correction,

$$p_{\ell m}^M(r) = \frac{4\eta_0}{3} s_{\ell m}(r) + \eta_0 \int_b^a \frac{\mathrm{d}}{\mathrm{d}r}\left[r\mathcal{D}_\ell K_\ell^M(r,r')\right] s_{\ell m}(r')\,\mathrm{d}r'. \tag{B 27}$$

At degree zero there is no tangential velocity and no biharmonic boundary correction. Impermeability requires

$$\int_b^a r^2 s_{00}(r)\,\mathrm{d}r = 0, \tag{B 28}$$

and the radial mass response may be written

$$U_{00}^M(r) = \frac{1}{r^2}\int_b^r t^2 s_{00}(t)\,\mathrm{d}t, \qquad p_{00}^M(r) = \frac{4\eta_0}{3} s_{00}(r). \tag{B 29}$$

The complete reference response is therefore

$$U_{\ell m}^{(v)} = U_{\ell m}^F + U_{\ell m}^M, \qquad V_{\ell m}^{(v)} = V_{\ell m}^F + V_{\ell m}^M, \qquad W_{\ell m}^{(v)} = W_{\ell m}^F, \tag{B 30}$$

which is the radial closed-form realization of the Green solution operator $\mathcal{G}_0$ used in Section 4.3. The ratio-scaled forms above involve only powers of radial ratios bounded by unity and satisfy the shell boundary conditions and source-radius matching conditions analytically.

Supplementary Material

The main paper contains the mathematical development, the principal validation results, and the physical interpretation of the spherical calculation. The purpose of this Supplementary Material is narrower. It records the numerical evidence used to establish convergence, spectral resolution, operator consistency, and reproducibility. The mathematical reason for the special treatment of degree one toroidal motion is developed in Appendix A of the main paper. Only its numerical audit is retained here.

Throughout this Supplement, a toroidal fraction means the fraction of the normalized squared velocity norm carried by the toroidal component. It is not a density weighted dimensional kinetic energy. Whenever an RMS toroidal to poloidal velocity ratio is quoted, it is the square root of the corresponding ratio of squared velocity norms.

S1. Iteration and numerical stopping measures

For prescribed viscosity, the transformed Stokes equations are linear in the velocity. The implementation evaluates the viscosity dependent contribution by a fixed point iteration in which an established reference Green operator is reused. If Z^k denotes the current spectral state and $\widetilde{Z}^{k+1}$ the state obtained from the newly evaluated effective load, the relaxed update is

$$Z^{k+1} = (1-\alpha)Z^k + \alpha\widetilde{Z}^{k+1}. \tag{S1}$$

The manufactured Cartesian benchmark uses $\alpha = 0.2$. The spherical calculations discussed below use $\alpha = 0.5$.

No single scalar residual is asked to carry the entire burden of certification. The state update measures convergence of the fixed point sequence. The transformed mass residual tests the corresponding mass constraint. The retained spectral tail measures activity near the highest solved degrees. The discarded source ratio measures the part of the newly generated effective load that would fall outside the retained angular space. These quantities answer different questions and are therefore reported separately.

The final contrast 10^4 calculation required 49 updates. Its final state change was 7.9514×10^{-9}. The operator consistent transformed mass residual was 2.4482×10^{-8}. The retained spectral tail was 2.9632×10^{-13}, and the discarded source ratio was 5.0886×10^{-12}.

S2. Radial refinement at viscosity contrast 10^3

The radial comparison uses the same $(L_\eta, m_\eta) = (16, 8)$ viscosity structure, the same degree two buoyancy forcing, the same angular truncation $L_{\max} = 144$, and the same relaxation parameter in both calculations. The only changes are $N_r = 129$ to 161 and the corresponding product quadrature order 129 to 161. Both calculations converged after 44 updates.

Representative results are listed in Table S1. The state norm changes by 6.7×10^{-8} in relative terms. The toroidal fraction of the renormalized velocity changes by 1.4×10^{-7}. The whole shell physical toroidal to poloidal ratio changes by 5.1×10^{-7}. At the surface, the total RMS speed changes by 1.2×10^{-8}, the divergence RMS by 2.6×10^{-8}, and the radial vorticity RMS by 2.8×10^{-7}. These differences are far smaller than the changes interpreted physically in Section 4.3 of the main paper.

This comparison was carried out at contrast 10^3, not at 10^4. It is therefore not presented as a second radial ladder at the largest contrast. Its purpose is to show that the radial representation has settled for a demanding member of the same model family. The final contrast 10^4 calculation uses the finer resolution $N_r = 161$.

Table S1. Radial refinement for the spherical calculation at viscosity contrast 10^3. The angular truncation is $L_{\max} = 144$ in both cases. The final column gives the relative change from $N_r = 129$ to $N_r = 161$.

Diagnostic	$N_r = 129$	$N_r = 161$	Relative change
Final state update	8.99543×10^{-9}	8.99509×10^{-9}	-3.78×10^{-5}
Operator consistent mass residual	3.17856×10^{-8}	3.17847×10^{-8}	-2.78×10^{-5}
Retained spectral tail	1.11517×10^{-11}	1.11517×10^{-11}	-1.23×10^{-7}
Discarded source ratio	2.84029×10^{-10}	2.84029×10^{-10}	1.37×10^{-6}
Renormalized toroidal fraction	3.45218×10^{-1}	3.45218×10^{-1}	-1.37×10^{-7}
State norm	5.54470×10^{-7}	5.54471×10^{-7}	6.72×10^{-8}
Physical whole shell T/P	1.45677×10^{-3}	1.45677×10^{-3}	-5.07×10^{-7}
Surface total RMS speed [cm yr^{-1}]	4.56317669	4.56317674	1.16×10^{-8}
Surface u_T/u_P RMS ratio	7.77894×10^{-2}	7.77894×10^{-2}	2.43×10^{-7}
Surface divergence RMS [rad/10 Myr]	$2.54923649 \times 10^{-1}$	$2.54923656 \times 10^{-1}$	2.58×10^{-8}
Surface radial vorticity RMS [rad/10 Myr]	$1.13474253 \times 10^{-1}$	$1.13474285 \times 10^{-1}$	2.82×10^{-7}

S3. Angular refinement at viscosity contrast 10^4

The contrast 10^4 calculation is more demanding in angular degree because successive evaluations of the viscosity dependent load can populate additional coupled modes. A calculation at $L_{\max} = 144$, denoted S3C, reached the state tolerance without difficulty. It nevertheless left a discarded source ratio of 1.5561×10^{-8}, slightly above the adopted 10^{-8} bandwidth criterion. The distinction is important. The fixed point sequence had converged, but the edge of the retained spectral space still lay too close to an active coupling pathway.

The calculation was repeated at $L_{\max} = 180$, denoted S4C, with $N_r = 161$ and quadrature order 161 unchanged. The retained spectral tail fell from 1.0763×10^{-9} to 2.9632×10^{-13}, a reduction by about 3.6×10^3. The discarded source ratio fell from 1.5561×10^{-8} to 5.0886×10^{-12}, a reduction by about 3.1×10^3. The state norm changed by only a few parts in 10^9, as did the toroidal fraction of the renormalized velocity. The warning at $L_{\max} = 144$ therefore diagnosed proximity to the truncation boundary rather than a material change in the resolved solution.

S4. Final physical reconstruction and operator checks

The final production calculation, S4, uses the same resolution as S4C and adds the complete coefficient output, physical velocity reconstruction, surface diagnostics, and maps. The physical velocity is analysed through degree 276, because multiplication by $e^{-\Lambda}$ broadens its harmonic content beyond the degree range solved directly for the reference problem.

The principal numerical checks are collected in Table S3. The generalized spherical harmonic round trip and the independent exact Green operator test lie close to floating point roundoff. The exact kernel boundary diagnostic is 6.58×10^{-17}. After physical reconstruction, the whole shell spectral tail is 3.88×10^{-14}.

The maximum round trip residual obtained by synthesizing and reanalysing the physical vector spherical harmonic field is larger, 2.43×10^{-7}. We report this value explicitly because the reconstructed field has much broader bandwidth than the reference solution. The corresponding Parseval residual is 3.50×10^{-14}, and the physical spectral tail remains

Table S2. Angular refinement of the contrast 10^4 spherical calculation. The radial resolution and product quadrature order are 161 in both cases. S3C and S4C omit the large physical map products so that the angular convergence of the spectral solution can be isolated economically.

Diagnostic	$L_{max} = 144$	$L_{max} = 180$
Final iteration	49	49
Final state update	8.31755×10^{-9}	7.95145×10^{-9}
Iteration mass indicator	3.40326×10^{-8}	3.33×10^{-8}
Retained spectral tail	1.07627×10^{-9}	2.96324×10^{-13}
Discarded source ratio	1.55610×10^{-8}	5.08859×10^{-12}
Renormalized toroidal fraction	$4.97620758 \times 10^{-1}$	$4.97620756 \times 10^{-1}$
State norm	$1.12338713 \times 10^{-6}$	$1.12338713 \times 10^{-6}$
Bandwidth warning	yes	no

Table S3. Numerical diagnostics for the final contrast 10^4 spherical calculation S4. The physical velocity is analysed through degree 276.

Diagnostic	Value
L_{max}	180
N_r	161
Product quadrature order	161
Physical analysis L_{max}	276
Fixed point updates	49
Final state update	$7.9514473104 \times 10^{-9}$
Operator consistent transformed mass residual	$2.4482103428 \times 10^{-8}$
Retained spectral tail	$2.9632410744 \times 10^{-13}$
Discarded source ratio	$5.0885877278 \times 10^{-12}$
Exact kernel boundary residual	$6.5814400180 \times 10^{-17}$
Generalized spherical harmonic round trip	$6.7590392146 \times 10^{-15}$
Exact Green operator test	$3.5527136788 \times 10^{-15}$
Global derivative consistency test	$1.4895512563 \times 10^{-12}$
Physical whole shell spectral tail	$3.8833968858 \times 10^{-14}$
Maximum physical VSH round trip residual	$2.4323477009 \times 10^{-7}$
Maximum physical VSH Parseval residual	$3.5038057526 \times 10^{-14}$

very small. The physical observables discussed in the main text are also stable under the independent radial and angular tests reported in Sections S2 and S3.

The radial viscosity profile is constructed so that its analytic radial derivative vanishes at both shell boundaries. A separate discrete derivative audit gives -1.28×10^{-11} at the inner boundary and 9.46×10^{-11} at the outer boundary in the nondimensional derivative used by the code. Forty three radial nodes lie across the principal support and full width measure of the viscosity profile, and fourteen lie across its surface transition. These counts provide a direct measure of how the imposed radial structure is represented on the $N_r = 161$ grid.

Table S4. Degree one toroidal and physical zero angular momentum diagnostics for the final S4 calculation.

Diagnostic	Value
Active azimuthal stride	8
Active degree one gauge dimension	1
Response matrix condition estimate	1.0000000000
Response inversion residual	$1.1102230246 \times 10^{-16}$
Final physical degree one moment norm	$4.9267981718 \times 10^{-24}$
Surface degree one radial vorticity [rad yr^{-1}]	$4.0095473267 \times 10^{-24}$
Surface differential rotation [deg Myr^{-1}]	$1.9895213689 \times 10^{-16}$

S5. Numerical audit of the degree one toroidal treatment

Appendix A establishes the mathematical distinction between torque compatibility and the physical zero angular momentum frame. The present section records how that distinction appears in the final numerical calculation.

The imposed $m = 0$ buoyancy and $m = 8$ viscosity field restrict the active azimuthal orders to multiples of eight. At degree one, only the $m = 0$ rotation therefore survives in the invariant subspace. The response matrix defined in Eq. (A 13) of the Appendix reduces to one dimension. Its condition estimate in S4 is 1.0, and the inversion residual is 1.11×10^{-16}.

The final physical degree one angular momentum norm is 4.93×10^{-24}. The associated surface differential rotation is 1.99×10^{-16} deg Myr^{-1}. The surface degree one radial vorticity is 4.01×10^{-24} rad yr^{-1}. These quantities are numerically negligible. The finite radial vorticity shown in Fig. 10(b) of the main paper is therefore not an arbitrary whole shell rotation introduced by the null mode.

The important point is what has not been removed. The frame correction is restricted to the exact rigid null coordinate of the reference problem. It does not delete the compatible degree one toroidal forcing, and it does not alter non-null coefficients. The numerical procedure therefore retains any physical differential rotation that the coupled problem may generate while fixing only the arbitrary rotational frame.

S6. Matched isoviscous control and run sequence

The matched control S0 was repeated at the same angular and radial resolution used for S4. The forcing, shell geometry, boundary conditions, reference viscosity, quadrature, and physical reconstruction are unchanged. The only physical change is that the amplitude of the lateral viscosity field is set to zero. Direct audits then give

$$\max|\Lambda| = 0, \qquad \max\left|\frac{\eta}{\eta_0} - 1\right| = 0, \qquad \max|\mathbf{v} - \mathbf{u}| = 0 \tag{S1}$$

at the precision written by the solver.

The maximum surface horizontal speed is 6.0346684 cm yr^{-1}, and the horizontal divergence RMS is 0.169448006 rad/10 Myr. The RMS divergence outside degree two is 3.34×10^{-13} rad/10 Myr, corresponding to 3.89×10^{-24} of the total divergence variance. The radial vorticity RMS is 1.68×10^{-13} rad/10 Myr. These values justify using S0 as a clean measure of the structure generated specifically by lateral viscosity variation.

Table S5. Calculations used in the spherical verification sequence. Q is the product quadrature order.

Run	Contrast	$L_{\max}$	N_r	Q	Purpose
S1	10^3	144	129	129	radial reference
S2	10^3	144	161	161	radial refinement
S3C	10^4	144	161	161	angular reference
S4C	10^4	180	161	161	angular refinement
S4	10^4	180	161	161	final physical solution
S0	1	180	161	161	matched isoviscous control

The maps in the main paper are also compared without independent colour renormalization. The isoviscous speed uses the same scale as the S4 physical speed, from zero to $10.3256\,\mathrm{cm\,yr^{-1}}$. The isoviscous divergence uses the same $[-1.5, +1.5]$ rad/10 Myr range as the S4 divergence.

Table S5 records the sequence of calculations used in the spherical certification. S1 and S2 isolate radial refinement at contrast 10^3. S3C and S4C isolate angular refinement at contrast 10^4. S4 is the final physical calculation, and S0 is its matched isoviscous control. The convergence calculations S3C and S4C omit the large map and coefficient products but solve the same fixed point spectral system.

Taken together, the tests answer three separate numerical questions. The radial comparison tests the representation of the radial operator and the imposed viscosity profile. The angular comparison tests whether successive viscosity couplings remain safely inside the retained harmonic space. The final reconstruction and degree one audit test whether the broadened physical field can be synthesized, analysed, and placed in a unique rotational frame without disturbing the resolved differential response. The interpretation in Section 4.3 of the main paper rests on the agreement of these independent checks rather than on any single residual.

References

Backus, George 1986 Poloidal and toroidal fields in geomagnetic field modeling. *Reviews of Geophysics* **24** (1), 75–109.

Backus, George E. 1958 A class of self-sustaining dissipative spherical dynamos. *Annals of Physics* **4**, 372–447.

Backus, George E. 1967 Converting vector and tensor equations to scalar equations in spherical coordinates. *Geophysical Journal of the Royal Astronomical Society* **13**, 71–101.

Belfort, Benjamin & Younes, Anis 2025 Semi-analytical solutions for flow with space or time-varying viscosity in fractured porous media. *Advances in Water Resources* **204**, 105041.

Blank, Bas, Barletta, Valentina Roberta, Hu, Haiyang X. S., Pappa, Folker & van der Wal, Wouter 2021 Effect of lateral and temporal viscosity variations on GIA-induced uplift rates in the Amundsen Sea Embayment. *ESS Open Archive* Preprint.

Čadek, Ondřej & Fleitout, Luce 2003 Effect of lateral viscosity variations in the top 300 km on the geoid and dynamic topography. *Geophysical Journal International* **152** (3), 566–580.

Čadek, O. & Fleitout, L. 2006 Effect of lateral viscosity variations in the core-mantle boundary region on predictions of the long-wavelength geoid. *Studia Geophysica et Geodaetica* **50** (2), 217–232.

Rodríguez de Castro, Antonio & Goyeau, Benoit 2021 A pore network modelling approach to investigate the interplay between local and Darcy viscosities during the flow of shear-thinning fluids in porous media. *Journal of Colloid and Interface Science* **590**, 446–457.

Christensen, Ulrich R. & Harder, Helmut 1991 3-d convection with variable viscosity. *Geophysical Journal International* **104** (1), 213–226.

Colin, P. 1993 Géoïde global, topographie associée et structure de la convection dans le manteau terrestre: modélisation et observations. Ph.d. thesis, École Normale Supérieure, Paris.

De Vanna, Francesco, Benato, Alberto, Picano, Francesco & Benini, Ernesto 2021 High-order conservative formulation of viscous terms for variable viscosity flows. *Acta Mechanica* **232** (6), 2115–2133.

Eberhard, U., Seybold, H. J., Secchi, E., Jiménez-Martínez, J., Rühs, P. A., Ofner, A., Andrade, J. S. & Holzner, M. 2020 Mapping the local viscosity of non-Newtonian fluids flowing through disordered porous structures. *Sci. Rep.* **10** (1).

Forte, Alessandro M. 2000 Seismic-geodynamic constraints on mantle flow: Implications for layered convection, mantle viscosity, and seismic anisotropy in the deep mantle. In *Earth's Deep Interior: Mineral Physics and Tomography from the Atomic to the Global Scale* (ed. Shun-ichiro Karato, Alessandro M. Forte, Robert C. Liebermann, Guy Masters & Lars Stixrude), *Geophysical Monograph Series*, vol. 117, pp. 3–36. Washington, DC: American Geophysical Union.

Forte, Alessandro M. 2007 Constraints on seismic models from other disciplines: Implications for mantle dynamics and composition. In *Treatise on Geophysics* (ed. Barbara Romanowicz & Adam M. Dziewonski), , vol. 1, pp. 805–858. Amsterdam: Elsevier.

Forte, Alessandro M. & Peltier, W. Richard 1987 Plate tectonics and aspherical earth structure: The importance of poloidal–toroidal coupling. *Journal of Geophysical Research: Solid Earth* **92** (B5), 3645–3679.

Forte, Alessandro M. & Peltier, W. Richard 1994 The kinematics and dynamics of poloidal–toroidal coupling in mantle flow: The importance of surface plates and lateral viscosity variations. In *Advances in Geophysics* (ed. Renata Dmowska & Barry Saltzman), , vol. 36, pp. 1–119. San Diego: Academic Press.

Jensen, Johan Ludwig William Valdemar 1906 Sur les fonctions convexes et les inégalités entre les valeurs moyennes. *Acta mathematica* **30** (1), 175–193.

Kaban, Mikhail K., Rogozhina, Irina & Trubitsyn, Valeriy 2007 Importance of lateral viscosity variations in the whole mantle for modelling of the dynamic geoid and surface velocities. *Journal of Geodynamics* **43** (2), 262–273.

Kamali Lima, Shayan 2026 Mantle rheology and earth dynamics: Spectral stokes modeling of isostatic response, lateral viscosity variations and surface geodynamic observables. PhD thesis, Université Paris Cité, Paris, France, doctoral dissertation, Institut de Physique du Globe de Paris; defended 1 June 2026.

Karato, Shun-ichiro 2008 *Deformation of Earth Materials: An Introduction to the Rheology of Solid Earth*. Cambridge: Cambridge University Press.

Karpychev, Mikhail & Fleitout, Luce 2000 Long-wavelength geoid: The effect of continental roots and lithosphere thickness variations. *Geophysical Journal International* **143** (3), 945–963.

Landau, Lev Davidovich & Lifshitz, Evgenii Mikhailovich 1987 *Fluid Mechanics: Volume 6*. Elsevier.

Lau, H. C. P., Austermann, J., Mitrovica, J. X., Crawford, O., Al-Attar, D. & Latychev, K. 2018 Inferences of Mantle Viscosity Based on Ice Age Data Sets: The Bias in Radial Viscosity Profiles Due to the Neglect of Laterally Heterogeneous Viscosity Structure. *Journal of Geophysical Research: Solid Earth* **123** (9), 7237–7252.

Moucha, R., Forte, A. M., Mitrovica, J. X. & Daradich, A. 2007 Lateral variations in mantle rheology: implications for convection related surface observables and inferred viscosity models. *Geophysical Journal International* **169** (1), 113–135.

Petrunin, A. G., Kaban, M. K., Rogozhina, I. & Trubitsyn, V. 2013 Revising the spectral method as applied to modeling mantle dynamics. *Geochemistry, Geophysics, Geosystems* **14** (9), 3691–3702.

Poirier, Jean-Paul 1985 *Creep of Crystals: High-Temperature Deformation Processes in Metals, Ceramics and Minerals*. Cambridge University Press.

Ribe, Neil M 1992 The dynamics of thin shells with variable viscosity and the origin of toroidal flow in the mantle. *Geophysical Journal International* **110** (3), 537–552.

Ricard, Yanick, Doglioni, Carlo & Sabadini, Roberto 1991 Differential rotation between lithosphere and mantle: A consequence of lateral mantle viscosity variations. *Journal of Geophysical Research: Solid Earth* **96** (B5), 8407–8415.

Richards, Mark A. & Hager, Bradford H. 1989 Effects of lateral viscosity variations on long-wavelength geoid anomalies and topography. *Journal of Geophysical Research: Solid Earth* **94** (B8), 10299–10313.

Rogozhina, Irina 2008 Global modeling of the effect of strong lateral viscosity variations on dynamic geoid and mantle flow velocities. Ph.d. thesis, Deutsches GeoForschungsZentrum GFZ, Potsdam, scientific Technical Report STR 08/08, 186 pp.

Zhang, Shuxia & Christensen, Ulrich R. 1993 Some effects of lateral viscosity variations on geoid and surface velocities induced by density anomalies in the mantle. *Geophysical Journal International* **114** (3), 531–547.

Zhong, Shijie, McNamara, Allen, Tan, Eh, Moresi, Louis & Gurnis, Michael 2008 A benchmark study on mantle convection in a 3-d spherical shell using citcoms. *Geochemistry, Geophysics, Geosystems* **9** (10).